The DOI for this manuscript is doi: 10.1175/JCLI-D-17-0382.1

Lubis, S., K. Matthes, N. Harnik, N. Omrani, and S. Wahl, 2018: Downward Wave Coupling between the Stratosphere and Troposphere under Future Anthropogenic Climate Change. J. Climate. doi:10.1175/JCLI-D-17-0382.1, in press.

Downward Wave Coupling between the Stratosphere and Troposphere under Future Anthropogenic Climate Change

Sandro W. Lubis *

Department of the Geophysical Sciences, University of Chicago, Chicago, Illinois, USA

GEOMAR Helmholtz Centre for Ocean Research Kiel, Kiel, Germany

Katja Matthes

GEOMAR Helmholtz Centre for Ocean Research Kiel, Kiel, Germany, and

Christian-Albrechts-Universität zu Kiel, Kiel, Germany

Nili Harnik

Department of Geophysics and Planetary Sciences, Tel Aviv University, Tel Aviv, Israel

Nour-Eddine Omrani

Geophysical Institute, University of Bergen and Bjerknes Centre for Climate Research, Bergen, Norway

Sebastian Wahl

GEOMAR Helmholtz Centre for Ocean Research Kiel, Kiel, Germany

* *Corresponding author address:* Sandro W. Lubis, Department of the Geophysical Sciences, University of Chicago, 5734 S Ellis Ave, Chicago IL 60637,USA. E-mail: slubis@uchicago.edu

ABSTRACT

Downward wave coupling (DWC) is an important process that characterizes the dynamical coupling between the stratosphere and troposphere via planetary wave reflection. A recent modeling study indicated that natural forcing factors, including sea-surface temperature variability and quasi-biennial oscillation, influence DWC and the associated surface impact in the Northern Hemisphere (NH). In light of this, we further investigate how DWC in the NH is affected by anthropogenic forcings, using a fully coupled chemistry-climate model CESM1 (WACCM). The results indicate that the occurrence of DWC is significantly suppressed in the future, starting later in the seasonal cycle, with more events concentrated in late winter (February-March). The future decrease in DWC events is associated with enhanced wave absorption in the stratosphere due to increased greenhouse gases. The enhanced wave absorption is manifest as more absorbing types of stratospheric sudden warmings, with more events concentrated in early winter. This early winter condition leads to a delay in the development of the upper stratospheric reflecting surface, resulting in a shift in the seasonal cycle of DWC towards late winter.

The tropospheric responses to DWC events in the future exhibit different spatial patterns compared to those of the past. In the North Atlantic sector, DWC-induced circulation changes are characterized by a poleward shift and an eastward extension of the tropospheric jet, while in the North Pacific sector, the circulation changes are characterized by a weakening of the tropospheric jet. These responses are consistent with a change in the pattern of DWC-induced synoptic-scale eddy-mean flow interaction.

1. Introduction

Vertical propagation of planetary waves represents one of the most fundamental processes involved in the linkage between the tropospheric and stratospheric circulation. Planetary waves are generated in the troposphere by orographic and/or non-orographic forcing and propagate upward into the stratosphere where they either break and induce a downward-propagating zonal-mean wind anomalies (e.g., Kodera et al. 1990; Baldwin and Dunkerton 2001, Lubis et al. 2018), or they are reflected downward toward the troposphere (Perlwitz and Harnik 2003). The heat and momentum transports via planetary waves are crucial in controlling key aspects of middle and high latitude climate, including the distribution of temperature and ozone, midlatitude tropospheric jet, and stratospheric westerlies.

In recent years evidence has accumulated that changes in the stratosphere can have a significant impact on the troposphere via downward planetary wave reflection from the stratosphere to the troposphere, known as downward wave coupling (DWC e.g., Perlwitz and Harnik 2003; Shaw et al. 2010; Shaw and Perlwitz 2013; Lubis et al. 2016a, 2017). DWC events occur when upward-propagating waves reach the stratosphere and then get reflected downward toward the troposphere, where they impact the wave and circulation (Perlwitz and Harnik 2003; Shaw et al. 2010; Lubis et al. 2016a, 2017). Many episodes of DWC are tied to the so-called bounded wave geometry of the stratospheric basic state, which is characterized by a vertical reflecting surface in the upper stratosphere and a well-defined high-latitude meridional waveguide in the lower stratosphere (e.g., Harnik and Lindzen 2001; Shaw et al. 2010; Lubis et al. 2016a, 2017). Recent research has revealed that DWC has a significant impact on the tropospheric circulation and surface climate over the North Atlantic region during midwinter (Shaw and Perlwitz 2013; Shaw et al. 2014; Dunn-Sigouin and Shaw 2015; Lubis et al. 2016a). DWC signals in the troposphere resemble a positive phase of the North-Atlantic Oscillation (NAO), characterized by a poleward tropospheric jet shift in the North Atlantic sector (Shaw and Perlwitz 2013; Dunn-Sigouin and Shaw 2015; Lubis et al. 2016a). This tropospheric circulation change is intimately linked to a net acceleration of the polar

vortex in the stratosphere, arising from the Eliassen-Palm (EP) flux divergence induced by DWC events (e.g., Dunn-Sigouin and Shaw 2015). More recently, Lubis et al. (2016a) showed that the tropospheric response to DWC is dominated by eddy-mean flow feedbacks which are excited by the initial downward wave reflection. In particular, following the wave-1 reflection in the stratosphere, a wave-1 geopotential height anomaly-like pattern emerges in the high latitude troposphere. This anomaly gives rise to increased winds in the high-latitude North Atlantic sector, as indicated by a poleward shift of the tropospheric jet, and an anomalous positive NAO-like response. This positive NAO-like response is further strengthened by synoptic-scale eddy feedback due to changes in lower level baroclinicity induced by increased vertical wind shear and SST forcing. Thus, a better knowledge of DWC and the involved mechanisms will help to improve the representation of tropospheric circulation and surface climate in climate models.

The influence of future anthropogenic climate change on the NH winter stratosphere has been discussed in great detail in model studies using 21st Century GHG emission scenarios (e.g., Charlton-Perez et al. 2008; Ayarzaguena et al. 2013; Manzini et al. 2014). Under the Representative Concentration Pathway (RCP) 8.5 scenario, Manzini et al. (2014) showed that the majority of CMIP5 models predict a weaker stratospheric zonal-mean wind at high latitudes in the NH winter. This result is supported by the majority of general circulation model (GCM) studies that show an increase in the frequency of SSW in response to increased GHG forcing (e.g., Butchart et al. 2000; Charlton-Perez et al. 2008; Bell et al. 2010; Ayarzaguena et al. 2013; Schimanke et al. 2013). One of the possible mechanisms that lead to such an increase is the upward shift in the location of critical layers, which leads to more waves penetrating and converging into the subtropical lower stratosphere, due to strengthening of the upper flanks of the subtropical jet (Shepherd and McLandress 2011). Other mechanisms are based on idealized model simulations, and show that an increased energy cascade from organization of baroclinic eddies (Tung and Orlando 2003) would cause enhanced upward propagation of large-scale planetary waves into the subtropical stratosphere (Eichelberger

and Hartmann 2005). Recent studies using an atmospheric chemistry-climate model (CCM) (Oberlnder et al. 2013; Ayarzaguena et al. 2013), show that a deepening of the Aleutian Low in response to climate change could also lead to enhanced upward wave propagation into the stratosphere, through positive interference of wave activity. The aforementioned studies have thus demonstrated a range of mechanisms by which upward-propagating waves lead to a weakening of the polar vortex under GHG-induced climate change. However the effect of DWC on the stratosphere and troposphere under future climate change in the NH, has never been considered. In this study, we extend these investigations by using a state-of-the-art chemistry climate model CESM1(WACCM), which has both a fully resolved stratosphere and a fully coupled ocean. In this way the significance of coupled ocean feedbacks in, for example, generating ocean-land contrasts and shaping the tropospheric response to DWC, as well as the importance of atmospheric chemistry for vortex variability are included.

Using a set of sensitivity simulations with CESM1(WACCM), consisting of a number of single natural forcing experiments (i.e., anthropogenic GHGs and ozone depleting substances (ODSs) are kept constant at 1960s levels), Lubis et al. (2016a) showed that natural forcing factors including SST and QBO are equally important in establishing a correct representation of DWC in the CCM. Excluding SST (QBO) forcing caused the DWC frequency to drop (increase) significantly. In addition, the QBO and SST variability also influence the tropospheric response to DWC, both through a modification of wave propagation and interaction with the mean flow in the stratosphere, and through a modification of the synoptic-scale eddy-mean flow feedbacks which are excited by the initial downward wave reflection (Lubis et al. 2016a). On the other hand, the role of anthropogenic forcing factors, including GHGs and ODSs on DWC, has so far only been examined in the SH (Shaw et al. 2011). Using a suite of NASA's Goddard Earth Observing System (GEOS) chemistry-climate model simulations, Shaw et al. (2011) showed that a significantly increased DWC in the SH spring, in the period of past ozone depletion can be attributed mainly to increased anthropogenic ODSs, while there is no significant change in the occurrence of DWC events in response to future

GHG forcing. However, the relative importance of theses anthropogenic forcing factors on DWC in the NH still remains unknown and will be addressed within this study.

The goal of the present study is to investigate the impact of future anthropogenic climate change on DWC in the NH winter stratosphere, particularly how their seasonality will change in the future, and how different anthropogenic forcings (GHG and ODSs) individually influence the occurrence of these events. We focus only on total planetary waves with zonal wave number 1, since it is the dominant source of DWC in the NH (Perlwitz and Harnik 2003). In addition, we also examine how these anthropogenic forcings can affect the downward influence of DWC on troposphere-surface climate in the future. To this end, we use different transient and timeslice simulations with a fully coupled chemistry climate model (CESM1[WACCM]) to investigate the impact of anthropogenic climate change on DWC and the underlying mechanisms. A description of the data, model experiments, and method is given in section 2. Section 3 describes the influence of future anthropogenic climate change on the background states, wave-mean flow interaction and DWC. In section 4, we assess the impact of DWC on future troposphere-surface climate over the North Atlantic and North Pacific sectors. The paper concludes with a summary and discussion in section 5.

2. Model, experiments, and methods

a. Model and experimental details

All simulations used in this study were performed within the National Center for Atmospheric Research (NCAR) Community Earth System Model (CESM) version 1.0.2, a fully coupled global Earth system model, which contains an interactive ocean, land, sea-ice, and atmosphere components (Gent et al. 2011; Hurrell et al. 2013). The Whole Atmosphere Community Climate Model (WACCM) version 4 (Marsh et al. 2013) is used for the atmosphere component with 66 standard vertical levels (up to 5.1×10^{-6} hPa or ~ 140 km) and the horizontal resolution of 1.9^0 latitude $\times$ 2.5^0 longitude. The model is coupled with inter-

active atmospheric chemistry, which is calculated within the 3-D chemical transport Model of Ozone and Related Chemical Tracers, Version 3 (MOZART-3; Kinnison et al. 2007). The model includes a total of 59 species, such as O_x, NO_x, HO_x, ClO_x, BrO_x, and CH_4, and 217 gas phase chemical reactions (Marsh et al. 2013). The interactive radiation and chemistry are implemented from the surface up to the lower thermosphere, so that some important processes in the middle atmosphere, such as ion chemistry, auroral processes, and nonlocal thermodynamic equilibrium radiation, are simulated (Marsh et al. 2013).

To investigate the influence of anthropogenic climate change on Northern Hemisphere DWC between the stratosphere and troposphere, we performed one long-term transient (TR) simulation with varying radiative forcings covering the period from 1955 to 2099 (145 years, Table 1). This simulation is forced with GHGs and ODSs following observations until 2005 and the RCP 8.5 scenario[1] (Meinshausen et al. 2011) out to the year 2100 (hereafter referred as the TR-RCP8.5 run). This simulation includes a representation of the QBO, implemented by relaxing equatorial zonal winds between 22°S and 22°N toward observation following Matthes et al. (2010) and extended into the future by projecting Fourier coefficients of the oscillation[2]. The solar spectral irradiance is specified as spectrally resolved daily variations obtained from the model of Lean et al. (2005). This simulation is run with interactive ocean and sea ice. In addition, a 145-yr control simulation (hereafter refer to CTRL run) is also used in which the model is run with fixed GHGs and ODSs at 1960s levels (i.e., no varying radiative forcing over the whole simulation period), so that the internal variability may be estimated. All other settings are equivalent to the TR-RCP8.5 simulation. Both model simulations (TR-RCP8.5 and CTRL) are initialized using initial files for January 1955 from a CESM-piControl experiment[3], from the CESM contribution to CMIP5, which runs for

[1]The radiative forcing reaches a maximum of ∼8.5 W m^{-2} in 2100.

[2]The QBO is projected into the future by developing Fourier coefficients for the QBO time series based on climatological values of Giorgetta (`http://www.pa.op.dlr.de/CCMVal/Forcings/qbo\data\ccmval\u_profile_195301-200412.html`) from the past records (1954-2004).

[3]http://www.cgd.ucar.edu/ccr/strandwg/CMIP5_experiment_list.html

several hundred years to reach an equilibrium state in the ocean. Future changes in DWC characteristics are assessed by comparing the last 40 winters of TR-RCP8.5 (2060-2099, "future") with the first 40 ones (1960-1999, "past").

We also employ different timeslice (TS) simulations of about 40 years with the same model which include separate changes in concentrations in GHG or ODS for present and projected future climate. TS simulations are climate model experiments which repeat all or most external forcings for a specific year while other follow a observed or projected record (e.g., Ayarzaguena et al. 2013). In our setup, the TS-GHG experiment uses seasonally varying surface emissions of ODSs at 1960s levels, in combination with surface emissions of GHGs at 2080s levels. As for the TS-ODS experiment, ODSs at 2080 levels in combination with surface emissions of GHGs at 1960s levels are used. All TS experiments are initialized using the background state from year 2080 of the TR-RCP8.5 run. All other external forcings (e.g. aerosols, NO2 aircraft emissions) are averaged +/-5 years around 2080 for both TS experiments. These sensitivity simulations allow us to isolate the influence of each anthropogenic forcing (GHG and ODS) on DWC. A detailed description of each TR and TS simulation is provided in Table 1.

b. Wave diagnostics

We use a time-lagged singular value decomposition (SVD) analysis to separate upward and downward propagating planetary wave signals between the stratosphere and troposphere (Perlwitz and Harnik 2003; Lubis et al. 2016a, 2017). This diagnostic isolates the leading coupled modes that represent the maximum covariance between two daily geopotential heights of zonal wavenumber k at two pressure levels (500 hPa and 10 hPa) for each time lag τ separately. The maximum relationship between the two wave fields is determined by the correlation of temporal expansion coefficients (A an B) of the leading coupled mode $\left[A^k(t), B^k(t+\tau)\right]$. The daily temporal expansion coefficients are calculated following Bretherton et al. (1992), in which each grid point data is linearly projected onto its

corresponding EOFs as:

$$A^k(t) = \sum_{i=1}^{M_p} V_i^k \, P_i \, (t) = \mathbf{V}_k^T \, P(t) \tag{1}$$

$$B^k(t+\tau) = \sum_{j=1}^{M_s} U_j^k \, S_j \, (t+\tau) = \mathbf{U}_k^T \, S(t+\tau). \tag{2}$$

where P and S signify daily tropospheric and stratospheric geopotential heights of zonal wavenumber k, respectively, and M indicates number of grid points. The left and right singular vectors at mode k are denoted by $\mathbf{V}_k$ and $\mathbf{U}_k$, respectively. We choose 500 hPa as a reference level, so that upward (downward) propagating wave is identified when the wave correlations are statistically significant at the positive (negative) time lags. Here, we are interested in the zonal wavenumber 1 because it is the dominant source of DWC in the NH (Perlwitz and Harnik 2003). We repeat the diagnostic for the entire seasons with 3-month overlapping periods as in Lubis et al. (2016a).

In addition, a diagnostic of the basic-state wave propagation characteristics (Harnik and Lindzen 2001; Lubis et al. 2016a, 2017) is used to determine the existence and location of reflecting surfaces for meridional and vertical wave propagation. This diagnostic is a more accurate indicator of wave propagation regions (rather than the index of refraction), since it diagnoses meridional and vertical propagation separately. For a non-isothermal atmosphere, the wavenumbers are diagnosed from the solution to the Rossby wave equation associated with the quasi-geostrophic (QG) conservation of potential vorticity (QG PV, Harnik and Lindzen 2001) (presented here for illustrative purposes in Cartesian coordinates):

$$\frac{\partial^2 \psi}{\partial z^2} + \frac{N^2}{f^2} \frac{\partial^2 \psi}{\partial y^2} + n_r^2 \psi = 0, \tag{3}$$

where, $\psi = \Phi / 2\Omega \sin\phi$ is geopotential streamfunction, Φ is geopotential, Ω is the rotation rate of the planet, N^2 is Brunt Vaisala frequency, f is Coriolis parameter, and n_r^2:

$$n_r^2 \equiv \frac{N^2}{f^2} \left\{ \frac{\bar{q}_y}{\overline{u} - c} - k^2 + f^2 \frac{e^{z/2H}}{N} \frac{\partial}{\partial z} \left[\frac{e^{-z/H}}{N^2} \frac{\partial}{\partial z} \left(e^{z/2H} N \right) \right] \right\} \equiv m^2 + \frac{N^2}{f^2} l^2. \tag{4}$$

Here, $\bar{u}$ is zonal mean wind, $\bar{q}_y$ is meridional gradient of zonal mean PV, H is scale height, k, and c are the zonal wavenumber and phase speeds, respectively. We focus on zonal wavenum-

ber 1 and set c to zero, so that we consider only stationary wavenumber 1. The coefficients of the wave Eq. (3) are calculated using monthly-mean zonal-mean zonal wind and temperature data. The vertical and meridional wavenumbers are subsequently diagnosed from the solution to the wave equation as $m^2 = -Re(\psi_{zz}/\psi)$ and $l^2 = -Re(\psi_{yy}/\psi)$, respectively (see Harnik and Lindzen 2001 for detailed theoretical considerations). A vertical reflecting surface for vertical wave propagation is the $m^2 = 0$ surfaces.

We also quantify the contribution of 3D planetary-scale wave flux (represented by $\mathbf{F_s}$ vectors, Plumb 1985, see appendix A) and 3D synoptic (transient) wave flux (represented by $\mathbf{E}$ vectors, Hoskins et al. 1983) on the mean flow. The 3D synoptic (transient) wave flux vectors $\mathbf{E}$ roughly point in the direction of the synoptic (baroclinic) wave energy propagation, and its convergence indicates deceleration of the zonal flow due to baroclinic wave forcing. The 3D synoptic-scale wave activities are computed as follows:

$$\mathbf{E} = \begin{Bmatrix} \overline{u'^2 - v'^2} \\ -\overline{v'u'} \\ -f\left(\frac{\partial\theta}{\partial p}\right)^{-1}\overline{v'\theta'} \end{Bmatrix}, \tag{5}$$

where v, θ, and p are the meridional wind, potential temperature and pressure level, respectively. The prime in $\mathbf{E}$ vectors denotes a 2-6 day band-pass Butterworth filtered daily anomaly, which represents the high frequency baroclinic wave activity (Blackmon 1976). The overbar signifies a time average. In addition, the upper-level storm-track activity is also analyzed, and is calculated as variance of 200-hPa meridional wind ($\overline{v'v'}$), which represents eddy activity aloft during a mature stage of the baroclinic eddy life cycle when perturbations are well developed (Wettstein and Wallace 2010).

c. Individual DWC Event Definition

An individual DWC event is identified based on the daily total negative wave-1 meridional heat flux ($\overline{v'T'}_{k=1}$) at 50 hPa weighted by the cosine of latitude and meridionally averaged between 60° and 90°N (Dunn-Sigouin and Shaw 2015; Lubis et al. 2016a). The DWC event

is defined when the $\overline{v'T'}_{k=1}$ at 50 hPa series drops below the 5th percentile of the January to March (JFM) distribution. The central date (day 0) is defined as the day of minimum $\overline{v'T'}_{k=1}$ and each event must be separated by at least 15 days. This time separation is motivated by the timescale of planetary wave coupling between the stratosphere and troposphere (Perlwitz and Harnik 2003). The $\overline{v'T'}_{k=1}$ is often negative after SSW events (Kodera et al. 2016) and such type of reflection is closely related to wave over-reflection (see Tomikawa 2010, for a detailed discussion). Therefore, in order to ensure that we only examine DWC events, we exclude from the reflection date event found above, those for which a SSW occurs within its duration or within 3-10 days after the onset of SSW events.

Qualitatively similar results are obtained for different choices of the reference level (e.g., $\overline{v'T'}_{k=1}$ at 30 and 10 hPa) or time seperation. The statistical significance of the DWC's life-cycle composites is calculated by performing a 1000-trial Monte Carlo analysis following Lubis et al. (2017). The anomalies for the composites are defined as the deviations from the daily climatological seasonal cycle.

3. Effect of climate change on DWC

In this section, the impact of future anthropogenic climate change on DWC is presented by first discussing this impact on the temperature, background wind, and wave-mean flow interaction. Then we diagnose the respective impacts on DWC by analyzing the wave coupling correlation and seasonal variation in wave geometries.

a. Stratospheric basic state responses

It is well established that the stratospheric basic states determine the transmission or refraction properties of vertically propagating planetary waves (Charney and Drazin 1961; Matsuno 1970). In turn, changes in the behavior of planetary waves can affect the basic states. Therefore, it is important to first examine how the temperature, background wind

and the propagation properties of planetary waves are changing in response to future anthropogenic climate change.

Figure 1 shows the zonal-mean temperature and zonal wind differences in the transient run (TR) between 40 winters in the recent past (1960-1999) and 40 winters at the end of the twenty-first century (2060-2099), which give a measure of the atmospheric response to an increase in GHG. We note that by the end of the twenty-first century ozone concentration has recovered to pre-ozone hole levels (Lubis et al. 2016b), so that the differences in the stratospheric response by this time can be primarily attributed to increased GHG levels. The change in stratospheric temperatures over the twenty-first century is characterized by a globally averaged stratospheric cooling (with magnitude of changes up to 12 K) and tropospheric heating (up to 5 K) (Figs. 1a-d). The maximum cooling takes place from November to January (NDJ) and is situated near the stratopause at 1 hPa where the stratospheric temperatures are highest. In addition, certain areas in the polar lower stratosphere are warmer (especially in DJF) that is consistent with increased SSW events in the future (not shown). However, the signal is not significant, which is likely due to high levels of variability in the polar northern latitudes, for example due to the presence of SSWs (Mitchell et al. 2012; Hansen et al. 2014). Bell et al. (2010) found that it was not the case for the idealized scenario of 4 times preindustrial CO_2, where the results become significant at these latitudes. The corresponding plot for the zonal winds (Figs. 1e-f) shows a deceleration of the stratospheric polar winds (up to 5 m/s), suggesting a more disturbed polar vortex. The maximum deceleration occurs during early winter to mid winter, from November to January, with magnitude up to 5 m/s, and gradually shifts upward and loses significance from February to April (FMA). In the troposphere, there is a poleward and upward shift of the tropospheric jet in response to increased in GHGs, across all seasons from NJF to FMA. These results are similar to most previous chemistry-climate model (CCM) studies using the RCP8.5 scenario and CMIP5 results (e.g., Mitchell et al. 2012; Ayarzaguena et al. 2013; Schmidt et al. 2013), although the peak of the maximum wind deceleration in the stratosphere from the previous

studies occurred somewhat late in mid winter from January-March. A possible reason for this discrepancy might be due to the competition of different contributors and the biases of each model to produce correct dynamical responses for the interaction between the stratosphere and GHGs or ozone changes (SPARC CCMVal 2010). The weakening of the polar vortex in response to future climate change would suggest an increase in wave absorption and a reduction in downward wave reflection in the stratosphere.

b. Wave-mean flow interaction responses

Figure 2 shows the three-month running mean differences of the EP-flux vector and the associated divergence. The EP-flux vector is a measure for the direction of planetary wave propagation and its divergence indicates the tendency of the zonal-mean flow in response to eddy forcing. From NDJ to DJF (Figs. 2a-b), there is a strong difference in the EP-flux at high latitudes (i.e., more upward propagation of planetary waves from the troposphere in the future) from the lower into the upper stratosphere. Therefore, more wave dissipation or absorption at high latitudes leads to a significant deceleration of stratospheric polar night jet (Figs. 1e-f). The EP-flux convergence anomalies in DJF is larger compared to NDJ, which is consistent with stronger stratospheric wind deceleration in DJF. Planetary waves propagating from the troposphere upward into the stratosphere become weaker in JFM with significant convergence anomalies mainly situated in the upper stratosphere and lower mesosphere (Fig. 2c). This behavior is consistent with significant easterly wind anomalies in the upper stratosphere and the equatorward shift of the easterly wind anomalies in the lower mesosphere in JFM (Fig. 1g).

The shift in the EP-flux convergence anomalies continues to evolve in late winter (Fig. 2d), but with significant values concentrated above 40 km. This is consistent with upward and equatorward shifts of easterly wind anomalies into the upper stratosphere in late winter (Fig. 1h). Furthermore, Figs. 2e-f show the differences of the zonal wave-1 EP-flux vector and its divergence from early winter to late winter. It can be seen that both pattern and

magnitude of EP-flux convergence from the total eddies (Figs. 2a-d) are to a large degree attributed to the wave-1 convergence anomalies (Figs. 2e-f). We also note that the high-latitude wave-1 EP-flux convergence is dominated by the vertical component (not shown).

In summary, the changes in EP-flux convergence from early to late winter are consistent with the magnitude of deceleration of the NH vortex winds in the future, which is strongest in early winter. This behavior may suggest a transition from stronger wave absorption in early winter to a weaker wave absorption in late winter in the future. We will discuss this implication on DWC further in the following section.

c. Seasonality of DWC events

We now analyze the impact of future climate change on the timing in the seasonal cycle of DWC, by first examining the wave coupling correlation and then the evolution of the wave geometry. Figure 3 shows three-month overlapping periods of lagged SVD correlations (rSVD) between geopotential heights of zonal wavenumber one (Z-ZWN1) at 500 and 10 hPa. Positive lags indicate upward downward wave propagation from the troposphere to the stratosphere, whereas negative lags indicate downward wave propagation (associated with wave reflection) from the stratosphere to the troposphere. These events are only considered if the signals are statistically significant at the 99% level (Perlwitz and Harnik 2003; Lubis et al. 2016a). In the recent past, there is significant downward wave propagation throughout the extended winter, as indicated by significant correlations at negative time lags from November to March (Fig. 3a). This period is somewhat longer compared to the observation, which mostly occur from January to March (e.g., Shaw et al. 2010; Lubis et al. 2016a). The downward wave activity maximizes at about 6-12 days from DJF to JFM. The time scales of downward propagation are also longer compared to the observations (e.g., Shaw et al. 2010; Lubis et al. 2016a), suggesting a slower downward group velocity of Z-ZWN1 from the stratosphere to the troposphere in the model. However, in the future, the downward wave events occur only over a shorter winter period from January to March, with no statistically

significant signals in early winter (Fig. 3b). The overall wave coupling correlations in the future are lower compared to the recent past, indicating a significant reduction of downward wave activity from the stratosphere to the troposphere.

To examine whether the changes in the future timing of downward wave activity obtained from the transient simulation are attributed mainly to GHGs, we repeated the same diagnostics for two 40-yr TS experiments with different combinations in prescribed future surface emissions of the ODSs and GHGs. The TS simulations suggest that weaker downward wave signals in the future are mainly due to increases in GHG forcing (Figs. 3c-d). In particular, in the experiment with future ODS changes only (TS-ODS), downward wave signals were notably more persistent over a longer period (from December through April, Fig. 3c), with a pattern resembling the seasonal variation of downward wave signals in the recent past. In contrast, a weak and less persistent downward wave signals were observed in the experiment with an increase in GHGs only (TS-GHG, Fig. 3d). We note that the high correlation in April to June for negative time lags in TS-GHG experiment is not related to downward wave signals, rather than to a non-linear wave reflection due to the vortex break up, since the vertical reflecting surface during this period (Fig. 4) is not bounded by the meridional waveguide (see Fig. S1d). The overall results suggest that a future decrease in the occurrence of downward wave activity in the NH is mainly attributed to increased GHG forcing alone, whereas ODS only play a minor role.

In order to ensure that the downward propagating wave signals found in Fig. 3 are associated with DWC events, we examine a month-to-month variation of the vertical reflecting surface and meridional waveguide. Note that the DWC occurs only when the vertical reflecting surface is bounded by a meridional waveguide in the lower stratosphere. Figure 4 shows the climatological vertical wavenumbers (m^2) averaged from 60 to 80^0N for both the TR-RCP8.5 and TS simulations. In the past, the stratospheric reflecting surface persists from early to late winter (October to March, Fig. 4a). This vertical reflecting surface is bounded by the extended meridional waveguide from November to March (Fig. S1a), allowing more

favorable conditions for the occurrence of DWC during this period. By combining the period of bounded wavegeometry and the wave coupling correlation, the active period of DWC in the past is from November to March. The significant downward wave correlations in October and April are not associated with DWC rather than due to nonlinear wave dynamics, for example, due to overreflection from a critical surface.

In the future, the vertical reflecting surfaces occur only from December to March (Fig. 4b), while the meridional waveguide exhibits the same seasonal evolution as in the past (Fig. S1b). This indicates that the favorable period for the DWC (based on the configuration of bounded wavegeometry) is from December to March. By combining the period of bounded wavegeometry and the wave coupling correlation, we can conclude that the active period of DWC in the future is only from January to March. We further show that, by using the TS simulations, the future changes in the reflecting surface are mainly attributed to GHG forcing (Fig. 4d), dominating the opposing influence of ozone recovery (Fig. 4c).

d. Mechanisms for changes in the seasonality of DWC events

The former analysis showed that there is a significant reduction of DWC events in the future, with a shift of their timing towards late winter (Fig. 3 and Fig. 4). To elucidate the mechanisms responsible for a decreased DWC activity in the future, we first analyze the trend in EP-flux divergence, vertical component of the EP-flux (Fz), and vertical wavenumbers in both transient warming and control simulations. We also analyze the frequency of SSW and heat flux events in order to better understand the effect of wave absorption on the mean flow.

Although there is a clear reduction of the future DWC signal from early to mid winter (Nov-Jan), the wave geometry shows a reflecting configuration (though the high latitude meridional waveguide is shallower during these months in the future (Fig. S1)). This suggests that wave geometry changes cannot explain the reduction in the wave-coupling correlation in Fig. 3 in general, nor in particular for the early winter conditions. To further examine this,

we analyze the trend in wave-1 EP-flux divergence, Fz, and vertical wavenumbers in NDJ as shown in Fig. 5. We do see that EP-flux wave-1 convergence is enhanced in the future (Fig. 5a). The increased wave convergence, in the first order, reflects increased wave absorption by the mean flow. Assuming there is no internal source of wave activity in the stratosphere, increased wave absorption simply results in reduction in downward wave reflection by the mean flow and thus, decreased DWC events. In addition, the strengthening of wave absorption is accompanied by enhanced upward wave propagation from the troposphere into the stratosphere, as indicated by a positive trend in Fz (see Fig. 5b), and by the positive trend in vertical wavenumber over the last decades, which altogether indicate a favorable condition for upward wave propagation in the future instead of downward reflection (Fig. 5c). This is again consistent with the wave coupling correlation in Figs. 3a-b, showing insignificant DWC events in early winter in the future. We also note that the future changes of m^2 in early winter are associated with changes in vertical shear of the zonal-mean wind (U_z) in the upper stratosphere. This is supported by a significant positive correlation between m^2, and U_z and $\bar{q}_y$ (see Table 2). In contrast to transient warming simulation, we found no significant trends from the control simulation, suggesting that increased wave absorption in the stratosphere is induced mainly by future anthropogenic forcing. Our results so far suggest that the significant reduction of DWC in the future, in particular during early winter, can be associated with enhanced wave absorption in the stratosphere (Fig. 2 and Fig. 5), with stronger absorption concentrated in early winter.

Nevertheless, one can argue that the basic state itself is, in turn, altered by the waves and thus affects DWC. For example, increased wave absorption in the future can lead to enhanced SSW events, and thus result in more downward wave reflection events. To investigate this possibility, we calculate the frequency of SSW events in the recent past and in the future from the TR-RCP8.5 simulation, and decompose these into reflective and absorptive types of SSW, following the definition of Kodera et al. (2016) (Figs. 6a-c). The reflective SSW is defined when the heat flux (zonal wavenumbers 1 averaged over 45-75^{0}N at 100 hPa) remains

negative for more than two out of seven days, on and after the maximum temperature during an SSW event, while the rest are classified as absorptive types. We found that there is a significant increase in SSW events in the future, compared to the past, where the frequency is dominated by absorptive SSW events (Figs. 6a-c). Thus, enhanced wave absorption in the future is mainly manifested by increased absorptive SSW events (rather than reflection), with more events concentrated in early winter. In addition, during absorptive SSW events, the vertical reflecting surface disappears, or is located higher in the upper stratosphere, compared to reflective SSW events that are located in the lower stratosphere (not shown). Thus, a delay in the development of the mid-stratospheric reflecting surface in the future could be associated with stronger absorptive SSW events in early winter. Furthermore, we also calculate the frequency of upward propagating wave events, which are defined by heat flux values (averaging over 45-75^{0}N at 100 hPa), exceeding the 90 percentile value of daily distribution. The events are further decomposed into long (short) wave pulse events. The long (short) wave pulse events are defined when the positive heat flux persists for more (less) than 10 days after the central date. Harnik (2009) showed that long pulses of the upward wave activity could potentially cause warming events, while short pulses could lead to reflection. Our results show that there is a significant increase in upward wave activity with long pulses in the future and with more events concentrated in early winter, from November to January. These results are, therefore, consistent with enhanced wave absorption, increased absorptive SSWs, and reduced DWC events in the future, with more events concentrated in early winter.

In summary, our results show that a future decrease in DWC events could, in general, be associated with enhanced wave absorption in the stratosphere. The enhanced wave absorption leads to more absorbing SSW events, with more events concentrated in early winter. This early winter condition could lead to a delay in the development of the upper stratospheric reflecting surface, resulting in a shift of the seasonal cycle of DWC towards late winter in the future.

4. Tropospheric impact of DWC in the future

Our previous results showed that DWC is weaker in the future, with a shift of their timing towards late winter. Here we examine whether the reduction of DWC events in the future has a potential impact on the tropospheric circulation and surface climate. We focus our analysis on the most active winter season JFM, as it is a favorable period for planetary wave coupling in the NH (e.g., Perlwitz and Harnik 2003; Lubis et al. 2016a, 2017) and as a period where both the recent-past and the future RCP8.5 experiments exhibit significant DWC signals in the troposphere, but weaker DWC activity in the future (see Figs. 3a-b).

a. Impact on the tropospheric circulation

Previous studies have shown that extreme negative wave-1 heat flux in the stratosphere can be used to isolate the tropospheric impacts of DWC (e.g., Dunn-Sigouin and Shaw 2015; Lubis et al. 2016a, 2017). In this study, the impact of individual DWC events on the tropospheric circulation is examined by looking at composites of various atmospheric and surface fields around the central events. The statistics of high-latitude wave-1 heat flux distribution for RCP8.5 simulation for the past and future periods are listed in Table 3. The 5th (95th) percentile values in Table 3 indicate the heat flux value below which 5% (95%) of each period's total heat flux distribution can be found. Consistent with our previous findings, there is a significant decreased (increased) downward (upward) wave activity in the future compared to the past. In particular, the wave-1 heat flux magnitude at the 5th percentile is lower by about 19.4% compared to the past, while the wave-1 heat flux at the 95th percentile is higher by 10.4% compared to the past.

Figure 7 shows the composites of 500-hPa geopotential height (a,d), 500-hPa zonal-mean wind (b,e), and mean sea level pressure (c,f) anomalies north of 20^0N during the time when DWC impact on the troposphere maximizes (days -3 to 3). In the past, the spatial pattern of the 500 hPa geopotential height and sea-level pressure anomalies resembles a clear wave-1

pattern with a node in the mid-latitudes. In particular, over the North Atlantic sector, the signals project more onto the positive phase of the NAO-like pattern (rather than onto the negative phase), which are characterized by a seesaw shape (a dipole pattern) between mid- and high latitudes (Fig. 7a). This signature is further illustrated in the composite 500 hPa zonal wind anomalies, which show a clear strengthening and poleward shift of the tropospheric jet over the North Atlantic basin (Fig. 7b). The corresponding sea-level pressure anomalies exhibit a zonally asymmetric structure similar to that of the 500 hPa geopotential height anomalies, being consistent with a quasi-barotropic, tropospheric NAO-like structure over the North Atlantic sector during the DWC events (Shaw and Perlwitz 2013). In addition, there are also significant signals in the North Pacific sector that reflect the potential impacts of wave reflection on the growth rate of baroclinic wave activity and the circulation over this region. The associated circulation change is characterized by an equatorward shift of the tropospheric jet. This result is consistent with the impact of DWC on tropospheric circulation obtained from reanalysis and model studies (e.g., Shaw and Perlwitz 2013; Shaw et al. 2014; Dunn-Sigouin and Shaw 2015).

In the future, the surface influence of DWC that resembles the tropospheric dipole-like pattern over the North Atlantic shifts eastward, relative to the patterns found in the past. In particular, the poleward shift of the tropospheric zonal-mean wind anomalies is located more to the east of the North Atlantic basin (Figs. 7e,h), which is consistent with the eastward shift of geopotential height anomalies at 500 hPa (Figs. 7d,g). Likewise, the dipole pattern in the sea-level pressure anomalies also shifts eastward (Figs. 7f,i). In the North Pacific, the easterly wind anomalies weaken substantially and extend more to the south compared to the past (Fig. 7h), suggesting a weakening of the westerlies on the equatorward flank of the jet in the future (see Fig. 9b later). These results are not sensitive to the DWC event definition or to the number of the events used for the composite calculation. In particular, if we randomly select the same number of composite members in the past as in the future, the differences in the spatial structures and magnitudes of the tropospheric responses to DWC

remain the same. Qualitatively similar results are found using the DJF winter season (not shown).

Interestingly, one might expect that the tropospheric and surface responses to DWC over the North Atlantic sector in the future will be weaker as a result of decreased DWC events. However, we found that the anomalous strength of the tropospheric response to DWC over this region is relatively similar to that of the past (e.g., by comparing the strength of the westerly wind anomalies in the past and in the future over the North Atlantic region), but with the patterns shifted to the east. In particular, the westerly anomaly center (over the North Atlantic sector) weakened significantly and shifted eastward into the Mediterranean. This suggests that other factors besides the frequency and strength of the downward wave propagation from the stratosphere to the troposphere influence the tropospheric response to DWC. A recent study by Lubis et al. (2016a) showed that internal tropospheric dynamics involving feedbacks from synoptic-scale eddy activity and atmosphere-ocean interaction were central to the responses, with the synoptic-scale eddy-driven accelerations being an order of magnitude larger than the directly induced planetary scale-driven accelerations. We thus proceed to examine those feedbacks in the following section.

b. Mechanisms of the tropospheric impact of DWC

In this section we aim to understand the dynamical mechanisms leading to the change in tropospheric DWC signal in the future. For this we examine the contribution of 3D synoptic-scale (baroclinic) waves and 3D planetary-scale waves on the mean flow similar to Lubis et al. (2016a).

Figure 8 shows the composites of the anomalous synoptic-scale divergence at 200 hPa, alongside the horizontal component of the **E** vectors (representing the influence of the synoptic-scale eddies on the horizontal large scale flow; Figs. 8a,d), anomalous vertical component of the **E** vectors at 775 hPa (representing the source of synoptic-scale eddies; Figs. 8b,e), anomalous synoptic meridional wind variance at 200 hPa (representing the

upper-level storm-track strength; Figs. 8c,f) and the synoptic Eady's growth rate (EGR) anomalies at 700 hPa (representing the baroclinic instability in the troposphere, Figs. 8d,h), for the past (top panel) and future (bottom panel). In the past, we see that the synoptic eddies induced accelerations, as shown by a divergence of **E** vectors, largely explain the poleward shift of the tropospheric wind anomalies over the North Atlantic sector (Fig. 8a and Fig. 7b). The magnitude of this acceleration is about ten times larger than those due to planetary-scale waves (see Fig. S2a in supplementary material). Consistent with Lubis et al. (2016a), the anomalous acceleration pattern induced by synoptic-scale eddy anomalies (Fig. 8a) is accompanied by poleward shift of the tropospheric synoptic wave source (Fig. 8b) and the associated storm track anomalies (Fig. 8c). These mean flow baroclinicity anomalies are consistent with a poleward shift of the EGR anomalies, which are mainly driven by changes in the vertical wind shear induced by DWC (see Figs. S4a-b in supplementary material). In the North Pacific, the convergence of synoptic-scale waves (Fig. 8a) mostly explains the easterly wind anomalies in this region (Fig. 7b). This anomalous deceleration pattern induced by synoptic-scale waves, as shown by a convergence of **E** vectors, is accompanied by a poleward shift of the negative tropospheric synoptic wave source (Fig. 8b) and the associated storm track anomalies (Fig. 8c).

In the future, the location of the synoptic-scale divergence over the North Atlantic shift to the east compared to the patterns observed in the recent past (Figs. 7a,b). This is consistent with the shift of the tropospheric flow responses to DWC over the North Atlantic sector (Figs. 7d-f). In particular, the synoptic wave divergence anomalies (divergence of **E** vectors) explain the peak of zonal wind anomalies over western Europe (Fig. 7e) and the extended pattern into eastern Europe. The magnitude of the synoptic eddy divergence is much larger than the accelerations by planetary-scale waves (see Fig. S2b in supplementary material), suggesting that synoptic-scale eddies play more important role in setting the tropospheric response to DWC in the future [consistent with the mechanism proposed by Lubis et al. (2016a)]. Furthermore, we also found that the eastward shift of the synoptic-

scale divergence over the North Atlantic sector is consistent with the shift of the tropospheric synoptic wave source (Fig. 8f), the storm track anomalies (Fig. 8g), and the lower level baroclinicity (Fig. 8h) to the east. The lower level baroclinicity anomalies in the future are attributed to both vertical wind shear and static stability, in contrast to the past that is driven mainly by vertical wind shear (see Figs. S3c-d in supplementary material). These results suggest that the tropospheric response to DWC over the North Atlantic sector in the future is associated with the eastward shift of the baroclinic eddy-mean flow interaction in response to anthropogenic climate change. In the North Pacific, the southward extension of easterly wind anomalies during DWC is consistent with the extension of the synoptic-scale wave convergences to the south (Fig. 8e). This anomalous deceleration is also consistent with the weakening of synoptic-scale wave activity and the storm track over the North Pacific in the future (Figs. 8f-g). The weakening of baroclinic wave activity is also consistent with decreased EGR in the western boundary of the North Pacific basin (Fig. 8h).

The results so far show that the tropospheric response to DWC events has a very different spatial pattern in the future, and that this change in pattern is similar for the mean flow quantities (zonal wind, surface pressure, and geopotential height) and for the synoptic eddies and their fluxes. This suggests that the tropospheric response to DWC is associated with a change in synoptic-scale eddy feedbacks. However, it is not clear why the pattern of the synoptic-scale eddy feedback differs compared to the past (i.e., shifting more to the east). Therefore, it is worth checking if changes in DWC-induced synoptic-scale eddy-mean flow interaction are adjusted by the changes in the mean states (both the mean flow and storm track) in response to future anthropogenic climate change.

To answer this question, we analyzed the differences in the JFM mean zonal wind ($\bar{u}$) and storm track ($\overline{v'v'}$) at 200 hPa between the future and the past (Fig. 9). In the North Atlantic, we can see that there is a poleward shift and an eastward extension of the $\bar{u}_{200}$ and $\overline{v'v'}_{200}$, alongside the associated **E** vectors in the future (Figs. 8a-c). The eastward extension of the mid-high latitude Atlantic eddy driven jet toward Western Europe is evident with peaks of

$\bar{u}_{200}$, $\overline{v'v'}_{200}$, and **E** vectors clearly shifting eastward compared to the climatology from the past (Figs. 9d-f). Similar patterns as shown in the responses (Figs. 8c,f) can be confirmed by a long-term linear trend for each quantity (see Fig. S4), where the trends in the North Atlantic tropospheric jet and the storm track altogether shift poleward and extend eastward. In the North Pacific sector, the poleward shift in the storm tracks and the tropospheric jet are also consistent with the DWC's response being confined to mid-high latitudes and with no subtropical extension in the Pacific in the future, whereas in the past there was a subtropical signal. These results suggest that the shift in the pattern of the DWC-induced synoptic-scale eddy-mean flow interaction in the mid-high latitude troposphere in the future is adjusted by the inherent changes in the mean states (both mean flow and storm track) in response to anthropogenic climate change.

The eastward extension of the North Atlantic storm track in the future in our model can be also related to changes in the lower level baroclinicity induced by local SST gradients, resulting in enhancing baroclinic wave activity and the associated impact on the mean flow. To test this hypothesis, we analyzed the differences in SST gradient and Eady's growth rate between future and past during winter JFM (Fig. 10). In Fig. 10, we can see that there is a weakening (strengthening) of SST gradient in the southern (middle) part of the Western Atlantic Gulf Stream front (Figs. 10a,b), which is consistent with the reduced (enhanced) EGR (Figs. 10c,d) end **E** vectors there (Figs. 9b,d). On the other hand, there is a strengthening of SST gradients to the east (around the North Sea) followed by enhanced EGR, suggesting an increased synoptic (baroclinic) wave generation over the North Sea and the Northwestern Europe (Figs. 9b,d). The strengthened baroclinicity over theses regions is consistent with the increased storm track and zonal wind (Figs. 9b,d). This provides a hint that the eastward extension of the North Atlantic jet under future climate change could be also related to the shift of the lower level baroclincity and the associated synoptic-scale eddy-mean flow interaction.

5. Summary and Discussion

This study examined the impact of future anthropogenic climate change on DWC in NH winter, particularly how their seasonality will change in the future, and how different anthropogenic forcings (GHG and ODSs) individually influence the occurrence of these events. Two long-term (145 years) fully coupled chemistry-climate model CESM1(WACCM) with fixed and time-varying anthropogenic forcings following the RCP8.5 scenario have been used to examine the impact of anthropogenic forcing on DWC. In addition, two TS experiments with a combination of past and future GHG or ODS concentrations were also used to isolate the influence of each anthropogenic forcing factor on DWC. In our analysis, the attribution of anthropogenic forcings on DWC was analyzed by examining the differences in background wind, wave-mean flow interaction, and a time-lagged vertical wave-1 coupling as well as the evolution of wave geometry. Furthermore, the tropospheric impact of DWC in midwinter was investigated using a metric based on the stratospheric heat flux extremes. Summary points from our analysis are as follows:

- There is a significant change in the vortex mean state over the twenty-first century, characterized by a weaker and more disturbed polar vortex, with most changes occurring in early winter (Fig.1). This is consistent with a significant increase in the EP-flux convergence during that period (Fig. 2).

- There is statistically significant change in DWC frequency and its seasonality over the twenty-first century, when compared to the recent past. In the past, DWC occurs throughout the winter, with most events concentrated in DJF, but as GHG concentrations increase, DWC becomes significantly weaker with more events concentrated in late winter, from February to March (Figs. 3a,b). Changes in GHG alone, without ODS's can account for these changes (Figs. 3c,d and Fig. 4).

- The future decrease in DWC events by the end of the twenty-first century could, in general, be associated with enhanced wave absorption in the stratosphere (Figs. 2, 5,

and 6). The enhanced wave absorption is manifest as more absorbing SSW events, with more events concentrated in early winter (Fig. 6). This early winter condition could lead to a delay in the development of the upper stratospheric reflecting surface during that period (Fig. 5), resulting in a shift in the seasonal cycle of the DWC towards late winter in the future.

- While the natural forcing factors, such as the SST variability and QBO, induce a change in the strength of the tropospheric response to DWC mostly over the North Atlantic (Lubis et al. 2016a), the increase in anthropogenic forcing (mainly due to GHG increases) changes the tropospheric response to DWC itself, with a large change in both ocean basins and a zonal shifting of the Atlantic center of action. This change in pattern is consistent with the trends in the climatology of the tropospheric jet and storm tracks, manifested as a shift in the main centers of eddy-mean flow interaction that shape the tropospheric response to DWC (Figs. 7 to Fig. 10).

A recent study by Lubis et al. (2016a), showed that the tropospheric response to DWC is dominated by eddy-mean flow feedbacks which are excited by the initial downward wave reflection. Thus, it is expected that an eastward shift of the storm track and jets will result in an eastward shift of the eddy feedbacks, and consistently of the tropospheric response to DWC in the future. It is also well established that the DWC induces strong positive NAO events (e.g., Lubis et al. 2016a; Shaw et al. 2014; Dunn-Sigouin and Shaw 2015) so that a reduction in downward reflection means a reduction in this source of positive NAO events. Our results, however, showed that while there is a significant reduction in DWC in the future, the strength of the NAO-like pattern does not significantly change, rather it induces an eastward extension of the positive NAO-like pattern. This suggests that other dynamical adjustments (outside of DWC) to global warming can be also important to determine the strength and dynamics of the NAO in the future.

We have yet to explain the mechanism that is responsible for the enhanced upward propagating planetary waves in our warming simulation. Previous studies have shown that

changes in the location of critical layers within the subtropical lower stratosphere cause an increase in upward propagating planetary waves from the troposphere into the stratosphere (Shepherd and McLandress 2011). In addition, recent studies have shown that such changes in planetary and synoptic wave breaking in the location of critical layers are mainly driving by tropical SSTs forcing (Oberlnder et al. 2013; Ayarzaguena et al. 2013). It is also argued that future increases in tropical SSTs can enhanced upward planetary wave activity into the stratosphere, through a positive interference of wave activity due to a deepening of the Aleutian Low (Ayarzaguena et al. 2013). Thus, it is possible that the increased upward wave activity with long pulses that causes an increase in wave absorption in the future, may be related to one of these processes. Further studies are required to check this possibility, and we leave this open for further investigation.

The results of the analysis also show that the North Atlantic storm track shifts poleward and extends farther east under future climate change, consistent with recent ocean-atmosphere coupled GCM studies (e.g., Woollings et al. 2012; Ciasto et al. 2016). Our model results suggest that the cause is likely due to the projected changes in local North Atlantic SST, resulting in intensification and extension of the eddy-driven jet towards western Europe. A recent study by Ciasto et al. (2016) found that such shift can be also due to the remote local SST changes, originating from the tropical western Pacific Ocean via Rossby wave trains. However, a clear attribution of that causality is difficult in our results because the analysis are performed on a fully coupled simulation. Therefore, further studies are required in order to better understand the origin of future changes in tropospheric jet shift in response to DWC (i.e., local versus remote influence); for example by performing a comprehensive set of sensitivity experiments with a separate climate forcing, such as tropical or subtropical SST-forcing only, sea-ice-forcing only, etc.

This work can be viewed as a complementary study to that of Lubis et al. (2016a), who specifically examined the impact of the natural forcing factors, including SST and QBO, on DWC and the associated surface impact in NH winter. In this study, we stressed

that anthropogenic forcing factors indeed play important roles in controlling DWC and the associated surface climate in the NH. Previous studies showed that 11-yr solar cycle may play a role in perturbing the stratospheric mean state and the formation of the reflecting surface in the upper stratosphere (Matthes et al. 2006; Lu et al. 2017a,b). Therefore, understanding the role of solar forcing for the tropospheric impact of DWC is important and a subject of future investigation. A better understanding of the dynamical processes by which the stratosphere can influence the troposphere via planetary wave reflection has the potential to improve seasonal forecasting and climate prediction, thus leading to significant societal impacts.

Acknowledgments.

We acknowledge support received from the German-Israeli Foundation for Scientific Research and Development under grant GIF1151-83.8/2011. This work has also been partially performed within the Helmholtz-University Young Investigators Group NATHAN funded by the Helmholtz-Association through the Presidents Initiative and Networking Fund and the GEOMAR Helmholtz Centre for Ocean Research Kiel. Part of the work was done while NH was on sabbatical at Stockholm university, supported by a Rossby Visiting Fellowship from the International Meteorological Institute (IMI) of Stockholm University, Sweden. We would also like to thank Ted Shepherd and Edwin Gerber for useful discussions on the results during their visit at the GEOMAR, Kiel. The model simulations were performed at the German Climate Computing Centre (Deutsches Klimarechenzentrum, DKRZ), Hamburg, and the NEC-HPC Linux Cluster at Christian-Albrechts Universität zu Kiel, Kiel.

APPENDIX A

Stationary Planetary Wave Forcing

To quantify the drag exerted by stationary planetary-scale waves on the zonal mean flow, the 3D wave activity flux (Plumb 1985) to diagnose the potential regional sources (sinks) and propagation characteristics of stationary planetary-scale wave activity is computed as follow:

$$\mathbf{F}_s = \frac{p\cos\phi}{p_o} \times \left\{ \begin{array}{l} \frac{1}{2a^2\cos^2\phi}\left[\left(\frac{\partial\psi'}{\partial\lambda}\right)^2 - \psi'\frac{\partial^2\psi'}{\partial\lambda^2}\right] \\ \frac{1}{2a^2\cos\phi}\left(\frac{\partial\psi'}{\partial\lambda}\frac{\partial\psi'}{\partial\phi} - \psi'\frac{\partial^2\psi'}{\partial\lambda\partial\phi}\right) \\ \frac{2\Omega^2\sin^2\phi}{N^2 a\cos\phi}\left(\frac{\partial\psi'}{\partial\lambda}\frac{\partial\psi'}{\partial z} - \psi'\frac{\partial^2\psi'}{\partial\lambda\partial z}\right) \end{array} \right\}, \tag{A1}$$

where λ, ϕ, Ω, and θ are the streamfunction, longitude, latitude, Earth's rotation rate, potential temperature, respectively, p is pressure level, and p_o is 1000 hPa. The overbar and prime in the $\mathbf{F_s}$ vectors denote the zonal mean and departure from it, respectively. The $\mathbf{F_s}$ vectors are parallel to the wave energy propagational direction and its zonal mean is equivalent to the Eliassen-Palm (EP) flux (James, 1994). The 3-D Plumb flux is calculated only for zonal-wave components of 1 to 2.

REFERENCES

Ayarzaguena, B., U. Langematz, S. Meul, S. Oberlnder, J. Abalichin, and A. Kubin, 2013: The role of climate change and ozone recovery for the future timing of major stratospheric warmings. *Geophysical Research Letters*, **40 (10)**, 2460–2465, doi:10.1002/grl.50477.

Baldwin, M. P. and T. J. Dunkerton, 2001: Stratospheric harbingers of anomalous weather regimes. *Science*, **294 (5542)**, 581–584, doi:10.1126/science.1063315.

Bell, C. J., L. J. Gray, and J. Kettleborough, 2010: Changes in northern hemisphere stratospheric variability under increased co2 concentrations. *Quarterly Journal of the Royal Meteorological Society*, **136 (650)**, 1181–1190, doi:10.1002/qj.633.

Blackmon, M. L., 1976: A climatological spectral study of the 500 mb geopotential height of the northern hemisphere. *Journal of the Atmospheric Sciences*, **33 (8)**, 1607–1623, doi:10.1175/1520-0469(1976)033⟨1607:ACSSOT⟩2.0.CO;2.

Bretherton, C. S., C. Smith, and J. M. Wallace, 1992: An intercomparison of methods for finding coupled patterns in climate data. *Journal of Climate*, **5 (6)**, 541–560, doi:10.1175/1520-0442(1992)005⟨0541:AIOMFF⟩2.0.CO;2.

Butchart, N., J. Austin, J. R. Knight, A. A. Scaife, and M. L. Gallani, 2000: The response of the stratospheric climate to projected changes in the concentrations of well-mixed greenhouse gases from 1992 to 2051. *Journal of Climate*, **13 (13)**, 2142–2159, doi:10.1175/1520-0442(2000)013⟨2142:TROTSC⟩2.0.CO;2.

Charlton-Perez, A. J., L. M. Polvani, J. Austin, and F. Li, 2008: The frequency and dynamics of stratospheric sudden warmings in the 21st century. *Journal of Geophysical Research: Atmospheres*, **113 (D16)**, n/a–n/a, doi:10.1029/2007JD009571, d16116.

734 Ciasto, L. M., C. Li, J. J. Wettstein, and N. G. Kvamst, 2016: North atlantic storm-track
735 sensitivity to projected sea surface temperature: Local versus remote influences. *Journal*
736 *of Climate*, **29 (19)**, 6973–6991, doi:10.1175/JCLI-D-15-0860.1.

737 Dunn-Sigouin, E. and T. A. Shaw, 2015: Comparing and contrasting extreme stratospheric
738 events, including their coupling to the tropospheric circulation. *Journal of Geophysical*
739 *Research: Atmospheres*, **120 (4)**, 1374–1390, doi:10.1002/2014JD022116, 2014JD022116.

740 Eichelberger, S. J. and D. L. Hartmann, 2005: Changes in the strength of the brewer-
741 dobson circulation in a simple agcm. *Geophysical Research Letters*, **32 (15)**, n/a–n/a,
742 doi:10.1029/2005GL022924, l15807.

743 Gent, P. R., et al., 2011: The community climate system model version 4. *Journal of Climate*,
744 **24 (19)**, 4973–4991, doi:10.1175/2011JCLI4083.1.

745 Hansen, F., K. Matthes, C. Petrick, and W. Wang, 2014: The influence of natural and
746 anthropogenic factors on major stratospheric sudden warmings. *Journal of Geophysical*
747 *Research: Atmospheres*, 2013JD021397, doi:10.1002/2013JD021397.

748 Harnik, N., 2009: Observed stratospheric downward reflection and its relation to up-
749 ward pulses of wave activity. *Journal of Geophysical Research: Atmospheres*, **114 (D8)**,
750 D08 120, doi:10.1029/2008JD010493.

751 Harnik, N. and R. S. Lindzen, 2001: The effect of reflecting surfaces on the vertical structure
752 and variability of stratospheric planetary waves. *Journal of the Atmospheric Sciences*,
753 **58 (19)**, 2872–2894, doi:10.1175/1520-0469(2001)058⟨2872:TEORSO⟩2.0.CO;2.

754 Hoskins, B. J., I. N. James, and G. H. White, 1983: The shape, propagation and mean-
755 flow interaction of large-scale weather systems. *J. Atmos. Sci.*, **40 (7)**, 1595–1612, doi:
756 10.1175/1520.

Hurrell, J. W., et al., 2013: The Community Earth System Model: A Framework for Collaborative Research. *Bull. Amer. Meteor. Soc.*, **94 (9)**, 1339–1360, doi:10.1175/BAMS.

Kinnison, D. E., et al., 2007: Sensitivity of chemical tracers to meteorological parameters in the MOZART-3 chemical transport model. *Journal of Geophysical Research: Atmospheres*, **112 (D20)**, D20 302, doi:10.1029/2006JD007879.

Kodera, K., H. Mukougawa, P. Maury, M. Ueda, and C. Claud, 2016: Absorbing and reflecting sudden stratospheric warming events and their relationship with tropospheric circulation. *Journal of Geophysical Research: Atmospheres*, **121 (1)**, 80–94, doi:10.1002/2015JD023359, 2015JD023359.

Kodera, K., K. Yamazaki, M. Chiba, and K. Shibata, 1990: Downward propagation of upper stratospheric mean zonal wind perturbation to the troposphere. *Geophysical Research Letters*, **17 (9)**, 1263–1266, doi:10.1029/GL017i009p01263.

Lean, J., G. Rottman, J. Harder, and G. Kopp, 2005: chap. SORCE Contributions to New Understanding of Global Change and Solar Variability, 27–53. Springer New York, doi:10.1007/0-387-37625-9_3.

Lu, H., L. J. Gray, I. P. White, and T. J. Bracegirdle, 2017a: Stratospheric response to the 11-yr solar cycle: Breaking planetary waves, internal reflection, and resonance. *Journal of Climate*, **30 (18)**, 7169–7190, doi:10.1175/JCLI-D-17-0023.1.

Lu, H., A. A. Scaife, G. J. Marshall, J. Turner, and L. J. Gray, 2017b: Downward wave reflection as a mechanism for the stratospheretroposphere response to the 11-yr solar cycle. *Journal of Climate*, **30 (7)**, 2395–2414, doi:10.1175/JCLI-D-16-0400.1.

Lubis, S. W., K. Matthes, N.-E. Omrani, N. Harnik, and S. Wahl, 2016a: Influence of the quasi-biennial oscillation and sea surface temperature variability on downward wave coupling in the northern hemisphere. *Journal of the Atmospheric Sciences*, **73 (5)**, 1943–1965, doi:10.1175/JAS-D-15-0072.1.

Lubis, S. W., N.-E. Omrani, K. Matthes, and S. Wahl, 2016b: Impact of the antarctic ozone hole on the vertical coupling of the stratosphere-mesosphere-lower thermosphere system. *Journal of the Atmospheric Sciences*, doi:10.1175/JAS-D-15-0189.1.

Lubis, S. W., V. Silverman, K. Matthes, N. Harnik, N.-E. Omrani, and S. Wahl, 2017: How does downward planetary wave coupling affect polar stratospheric ozone in the arctic winter stratosphere? *Atmospheric Chemistry and Physics*, **17 (3)**, 2437–2458, doi:10.5194/acp-17-2437-2017.

Manzini, E., et al., 2014: Northern winter climate change: Assessment of uncertainty in cmip5 projections related to stratosphere-troposphere coupling. *Journal of Geophysical Research: Atmospheres*, **119 (13)**, 7979–7998, doi:10.1002/2013JD021403.

Marsh, D. R., M. J. Mills, D. E. Kinnison, J.-F. Lamarque, N. Calvo, and L. M. Polvani, 2013: Climate change from 1850 to 2005 simulated in CESM1 (WACCM). *Journal of Climate*, **26 (19)**, 7372–7391, doi:10.1175/JCLI-D-12-00558.1.

Matthes, K., Y. Kuroda, K. Kodera, and U. Langematz, 2006: Transfer of the solar signal from the stratosphere to the troposphere: Northern winter. *Journal of Geophysical Research: Atmospheres*, **111 (D6)**, n/a–n/a, doi:10.1029/2005JD006283, d06108.

Matthes, K., D. R. Marsh, R. R. Garcia, D. E. Kinnison, F. Sassi, and S. Walters, 2010: Role of the QBO in modulating the influence of the 11 year solar cycle on the atmosphere using constant forcings. *Journal of Geophysical Research: Atmospheres*, **115 (D18)**, D18 110, doi:10.1029/2009JD013020.

Meinshausen, M., et al., 2011: The rcp greenhouse gas concentrations and their extensions from 1765 to 2300. *Climatic Change*, **109 (1)**, 213–241, doi:10.1007/s10584-011-0156-z.

Mitchell, D. M., S. M. Osprey, L. J. Gray, N. Butchart, S. C. Hardiman, A. J. Charlton-Perez, and P. Watson, 2012: The effect of climate change on the variability of the northern

hemisphere stratospheric polar vortex. *Journal of the Atmospheric Sciences*, **69 (8)**, 2608–2618, doi:10.1175/JAS-D-12-021.1.

Oberlnder, S., U. Langematz, and S. Meul, 2013: Unraveling impact factors for future changes in the brewer-dobson circulation. *Journal of Geophysical Research: Atmospheres*, **118 (18)**, 10,296–10,312, doi:10.1002/jgrd.50775.

Perlwitz, J. and N. Harnik, 2003: Observational evidence of a stratospheric influence on the troposphere by planetary wave reflection. *Journal of Climate*, **16 (18)**, 3011–3026, doi:10.1175/1520-0442(2003)016⟨3011:OEOASI⟩2.0.CO;2.

Plumb, R., 1985: On the Three-Dimensional Propagation of Stationary Waves. *J. Atmos. Sci.*, **42 (3)**, 217–229, doi:10.1175/1520.

Schimanke, S., T. Spangehl, H. Huebener, and U. Cubasch, 2013: Variability and trends of major stratospheric warmings in simulations under constant and increasing ghg concentrations. *Climate Dynamics*, **40 (7-8)**, 1733–1747, doi:10.1007/s00382-012-1530-x.

Schmidt, H., et al., 2013: Response of the middle atmosphere to anthropogenic and natural forcings in the cmip5 simulations with the max planck institute earth system model. *Journal of Advances in Modeling Earth Systems*, **5 (1)**, 98–116, doi:10.1002/jame.20014.

Shaw, T. A. and J. Perlwitz, 2013: The life cycle of Northern Hemisphere downward wave coupling between the stratosphere and troposphere. *Journal of Climate*, **26 (5)**, 1745–1763, doi:10.1175/JCLI-D-12-00251.1.

Shaw, T. A., J. Perlwitz, and N. Harnik, 2010: Downward wave coupling between the stratosphere and troposphere: The importance of meridional wave guiding and comparison with zonal-mean coupling. *Journal of Climate*, **23 (23)**, 6365–6381, doi:10.1175/2010JCLI3804.1.

Shaw, T. A., J. Perlwitz, N. Harnik, P. A. Newman, and S. Pawson, 2011: The impact of stratospheric ozone changes on downward wave coupling in the Southern Hemisphere. *Journal of Climate*, **24 (16)**, 4210–4229, doi:10.1175/2011JCLI4170.1.

Shaw, T. A., J. Perlwitz, and O. Weiner, 2014: Troposphere-stratosphere coupling: Links to North Atlantic weather and climate, including their representation in CMIP5 models. *Journal of Geophysical Research: Atmospheres*, **119 (10)**, 5864–5880, doi:10.1002/2013JD021191.

Shepherd, T. G. and C. McLandress, 2011: A robust mechanism for strengthening of the brewerdobson circulation in response to climate change: Critical-layer control of subtropical wave breaking. *Journal of the Atmospheric Sciences*, **68 (4)**, 784–797, doi:10.1175/2010JAS3608.1.

SPARC CCMVal, 2010: SPARC report on the evaluation of chemistry-climate models. *SPARC-Report No.5, WCRP-132, WMO/TD-No. 1526*.

Tomikawa, Y., 2010: Persistence of easterly wind during major stratospheric sudden warmings. *Journal of Climate*, **23 (19)**, 5258–5267, doi:10.1175/2010JCLI3507.1.

Tung, K. K. and W. W. Orlando, 2003: The k3 and k5/3 energy spectrum of atmospheric turbulence: Quasigeostrophic two-level model simulation. *Journal of the Atmospheric Sciences*, **60 (6)**, 824–835, doi:10.1175/1520-0469(2003)060⟨0824:TKAKES⟩2.0.CO;2.

Wettstein, J. J. and J. M. Wallace, 2010: Observed patterns of month-to-month storm-track variability and their relationship to the background flow. *Journal of the Atmospheric Sciences*, **67 (5)**, 1420–1437, doi:10.1175/2009JAS3194.1.

Woollings, T., J. M. Gregory, J. G. Pinto, M. Reyers, and D. J. Brayshaw, 2012: Response of the north atlantic storm track to climate change shaped by ocean-atmosphere coupling. *Nature Geosci*, **5 (5)**, 313–317, doi:10.1038/ngeo1438.

List of Tables

TABLE 1. Description of CESM1(WACCM) transient and timeslice experiments. All experiments are run with QBO nudging and with interactive chemistry and SSTs/sea ice. TR= transient run and TS = timeslice run.

Experiment	Period	GHG	ODS
CTRL	1955-2099 (145 years)	fixed at 1960s level	fixed at 1960s level
TR-RCP8.5	1955-2099 (145 years)	Obs+RCP8.5[a]	Obs+RCP8.5[a]
TS-ODS	40 years	fixed at 2080 level	fixed at 1960s level
TS-GHG	40 years	fixed at 1960s level	fixed at 2080s level

[a]GHG/ODS follows observations until 2005 and the RCP8.5 scenario thereafter.

TABLE 2. Statistical features of the November to December 60-80°N means of the 5-1 hPa mean m^2 and the 10-1 hPa means of zonal-mean wind shear (U_z) and curvature (U_{zz}), Brunt Vaisalla frequency (N^2), and meridional gradient of potential vorticity ($\overline{q}_y$). Correlations significant at the 95% level based on a two-sided student t test, assuming each year is independent, are in bold.

Variables	Correlation with $\langle m^2 \rangle$	$\lvert t \rvert_{val}$	prob
$\langle m^2 \rangle$	1.000	∞	1.00
$\langle U_z \rangle$	**0.379**	3.98	0.99
$\langle U_{zz} \rangle$	-0.185	1.05	0.53
$\langle N^2 \rangle$	0.004	0.05	0.39
$\langle \overline{q}_y \rangle$	**0.316**	3.48	0.96

TABLE 3. Statistics of the daily distribution of wave-1 heat flux averaged from 60 to 90°N at 50 hPa during JFM from the TR-RCP8.5 experiment for the past and future periods.

Period	Mean	Std dev	5th Percentile	95th Percentile	KS test p value
Past	18.66	24.43	-13.94	60.51	1.00
Future	20.41	25.11	-11.23	67.50	0.04

List of Figures

889 4 The climatological vertical wavenumbers (m) averaged between 60-80°N for
890 (a) TR-RCP8.5 past (1960-1999), (b) TR-RCP8.5 future (2060-2099), and
891 two timeslice experiments with (c) future ODSs forcing and (d) future GHG
892 forcing. The vertical wavenumbers (units 10^{-5} m^{-1}) are contoured with 0.01
893 (thick line); 2, 4 (dashed line); 6-30 in jumps of 3 (thin lines). Finally, the
894 shading indicates the regions of wave evanescence in vertical directions ($m <$
895 0). The red solid lines indicate the approximate linear descent rate of vertical
896 reflecting surface. 44

897 5 Nov-Jan (NDJ) mean of (a) wave-1 EP-flux divergence averaged over 10-
898 0.1 hPa and 60-80°N, (b) vertical component of EP-flux vectors at 100 hPa
899 averaged over 40-70°N and (c) vertical wavenumbers averaged over 5-1 hPa
900 and 60-80°N, from the TR-RCP8.5 (red) and CTRL (green) simulations. The
901 straight dashed lines indicate linear best-fit regression (trend). 45

902 6 The frequency of major warmings and upward heat flux events in NH winter
903 months in TR-RCP8.5 simulation for the past (1960-1999, orange) and the
904 future (2060-2099, darkgreen). (a) total frequency of major warming events
905 and their decomposition into (b) absorptive and (c) reflective events. (d)
906 the frequency of upward heat flux ($\overline{v'T'}$ >0) events at 100 hPa and their
907 decomposition into (e) upward waves with long pulses and (f) with short
908 pulses. The horizontal dashed lines indicate the mean of the frequency. 46

7 The composites of (a,d) 500-hPa geopotential height (Z500), (b,e) 500-hPa zonal wind (U500), and (c,f) mean sea level pressure (MSLP) anomalies during the period of maximum DWC impact on the troposphere (days -3 to 3) in JFM for (top) TR-RCP8.5 past (1960-1999) and (bottom) TR-RCP8.5 future (2060-2099). (g-i) The difference between the future and the past of the respective anomalies. Contour interval is 10 m for Z500, 1 m/s for U500, and 1 hPa for MSLP. The zero contour is omitted. The color shadings are only drawn for anomalies that are statistically significant at the 95% confidence level according to a 1000-trial Monte Carlo test. 47

8 The composites of (a,e) 200 hPa synoptic wave divergence, (b,f) 775 hPa synoptic wave source, (c,g) 200 hPa storm track, and (d,h) 700-hPa Eady's growth rate anomalies during the period of maximum DWC impact on the troposphere (days -3 to 3) in JFM, for (top) TR-RCP8.5 past (1960-1999) and (bottom) TR-RCP8.5 future (2060-2099). The vectors indicate horizontal component of **E** vectors (Fx, Fy) at 200 hPa. The vertical component of **E** vectors in (b,f) is calculated by $-f\overline{v'\theta'}(\partial\theta/\partial p)^{-1}$ representing the synoptic wave source, where the positive (negative) values indicate upward (downward) synoptic wave fluxes. The color shading in (c,g) indicates the upper-level storm track anomalies ($\overline{v'v'}$) at 200 hPa. The Eady maximum growth rate is calculated as $0.31|f||\partial u/\partial z|/N$. The shadings are only drawn for anomalies that are statistically significant at the 95% confidence level according to a 1000-trial Monte Carlo test. 48

9 Winter mean (JFM) 200-hPa zonal wind and 200-hPa storm track ($\overline{v'v'}$) from (a,c) the past and (b,d) the response (future-past) from RCP8.5 simulation (TR-RCP8.5). The black contour lines in (c,f) indicate a climatology from the past. The gray dots indicate the regions where the changes are significant at the 95% confidence level according to a two-tailed t test. 49

936 10 Winter mean (JFM) meridional gradient of SST (SSTy) and Eady's growth
937 rate maximum (EGR) at 925 hPa from (a,c) the past and (b,d) the response
938 (future-past) in coupled RCP8.5 simulation (TR-RCP8.5). The gray shading
939 regions indicate where the land or the "underground" grid points (i.e. z
940 $>$ 1 km) have been excluded from the analysis. The SSTy value has been
941 multiplied by minus one for a better comparison with the EGR's sign. The
942 gray dots indicate the regions where the changes are significant at the 95%
943 confidence level according to a two-tailed t test.

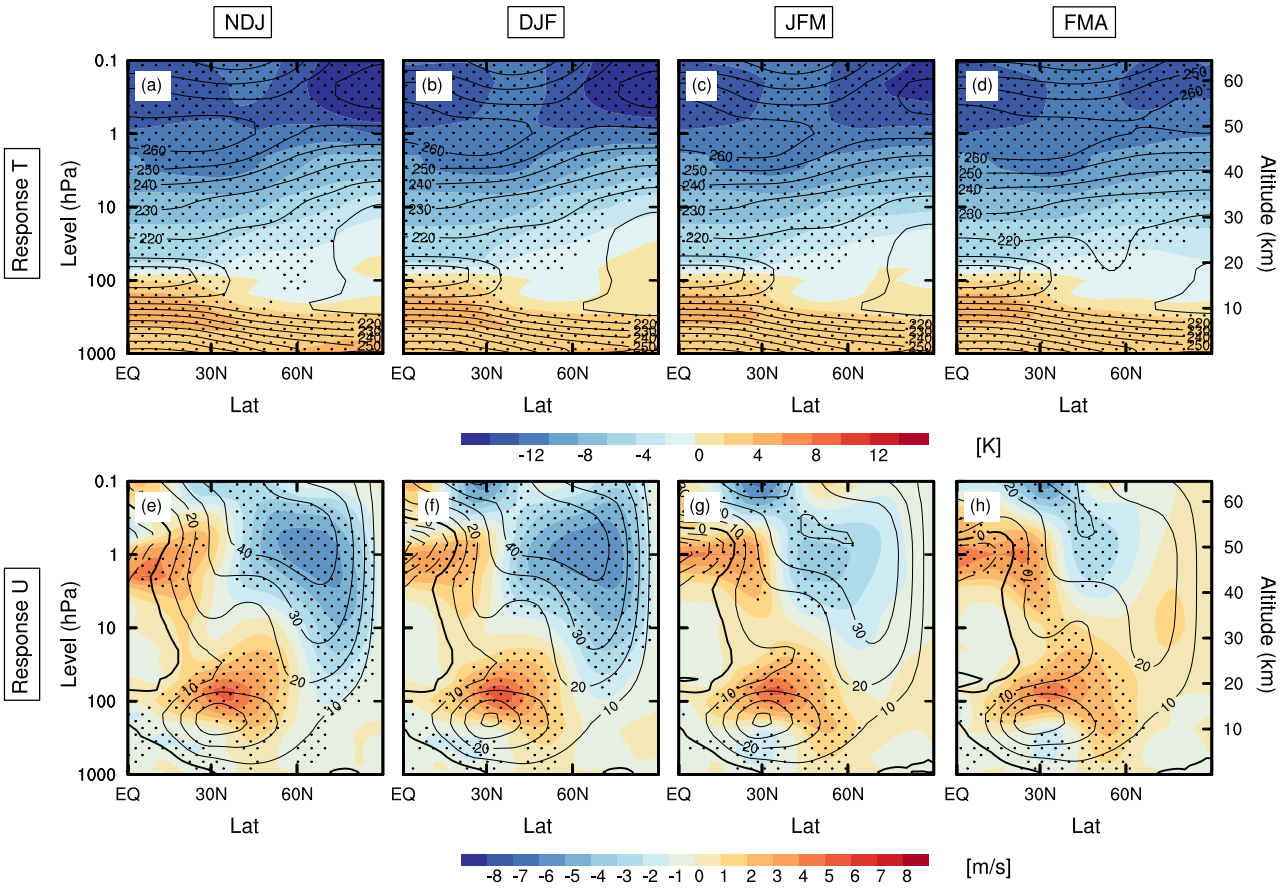

FIG. 1. Differences in the (a-d) zonal-mean temperature and (e-h) zonal-mean wind between the past (1960-1999) and future (2060-2099) climatologies for the transient TR-RCP8.5 run during (left to right) NDJ, DJF, JFM, and FMA. The black contour lines indicate the climatology from the CTRL run. The temperature responses use contour intervals of 2 K; for the zonal wind responses the contour interval is 1 m/s. Contour intervals from the CTRL are 10 K and 10 m/s for the temperature and zonal wind climatologies, respectively. Dotted areas indicate regions where the signal are statistically significant at the 95% level according to a two-tailed t test.

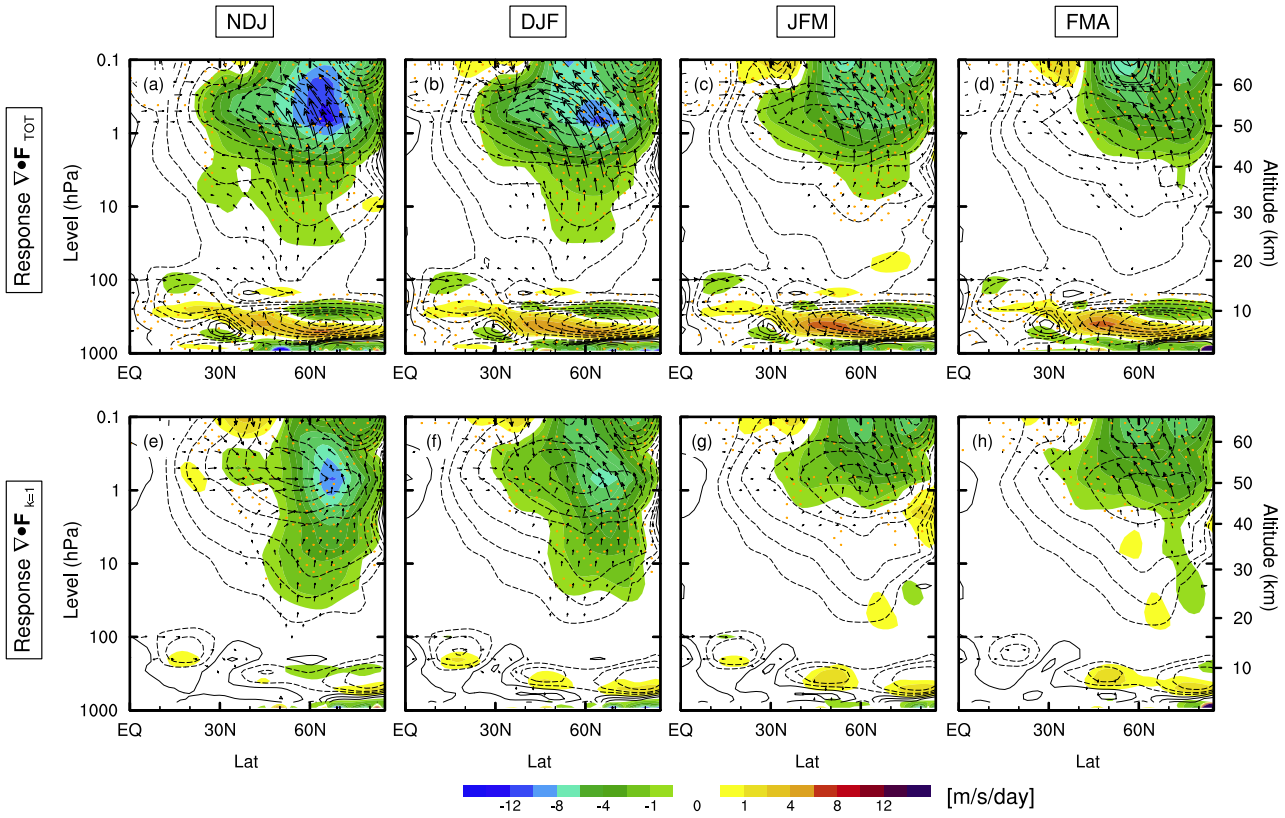

FIG. 2. Differences in the (a-d) total and (e-h) wave-1 EP-flux vectors between the past (1960-1999) and future (2060-2099) climatologies, as well as the corresponding differences in EP-flux divergence (shadings), from the transient TR-RCP8.5 run during (left to right) NDJ, DJF, JFM, and FMA. The black contour lines indicate the climatology of EP-flux divergence from the CTRL run. The contour intervals are in logarithmic powers of 2: $\pm$ [0.5, 1, 2, 4, 8, 16, 32, 64,..] m s^{-1} day^{-1}. Dotted areas indicate regions where the signal are statistically significant at the 95% level according to a two-tailed t test.

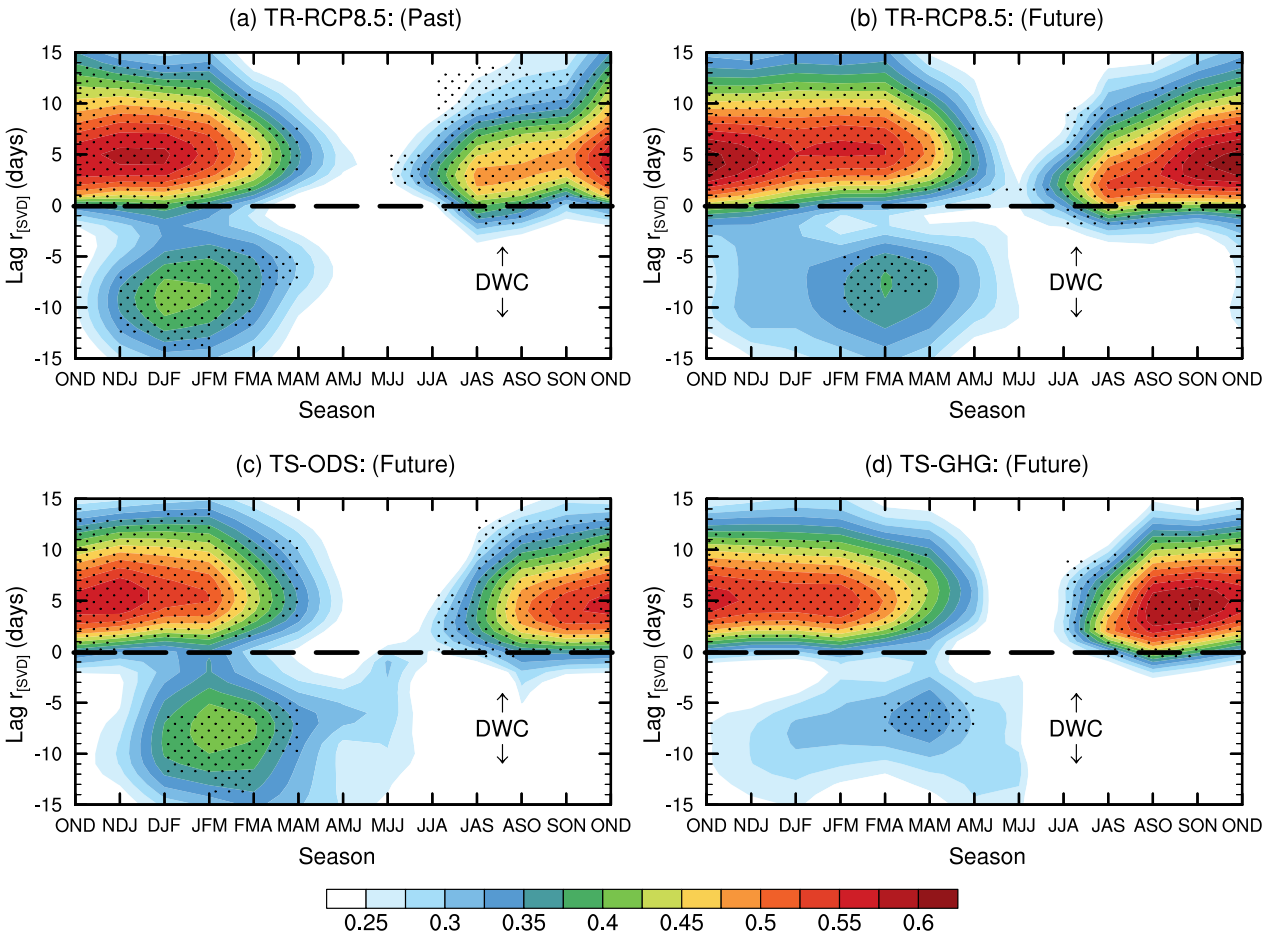

FIG. 3. Three-month overlapping periods of lagged SVD correlations between wave-1 geopotential height (Z-ZWN1) at 500 hPa and 10 hPa for (a) TR-RCP8.5 past (1960-1999), (b) TR-RCP8.5 future (2060-2099), and two timeslice experiments with (c) future ODSs forcing and (d) future GHG forcing. Solid dots represent values significant at the 99% level. A negative (positive) time lag indicates that the stratospheric (tropospheric) wave field is leading.

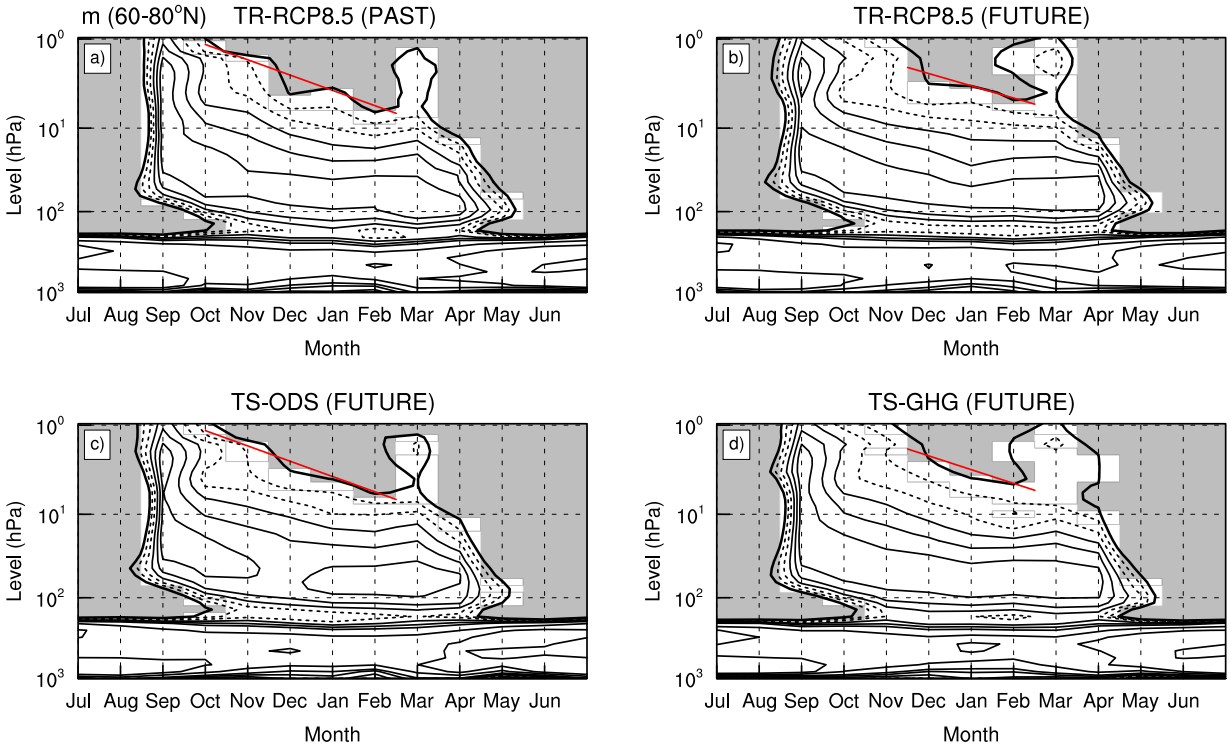

FIG. 4. The climatological vertical wavenumbers (m) averaged between 60-80°N for (a) TR-RCP8.5 past (1960-1999), (b) TR-RCP8.5 future (2060-2099), and two timeslice experiments with (c) future ODSs forcing and (d) future GHG forcing. The vertical wavenumbers (units 10^{-5} m^{-1}) are contoured with 0.01 (thick line); 2, 4 (dashed line); 6-30 in jumps of 3 (thin lines). Finally, the shading indicates the regions of wave evanescence in vertical directions ($m < 0$). The red solid lines indicate the approximate linear descent rate of vertical reflecting surface.

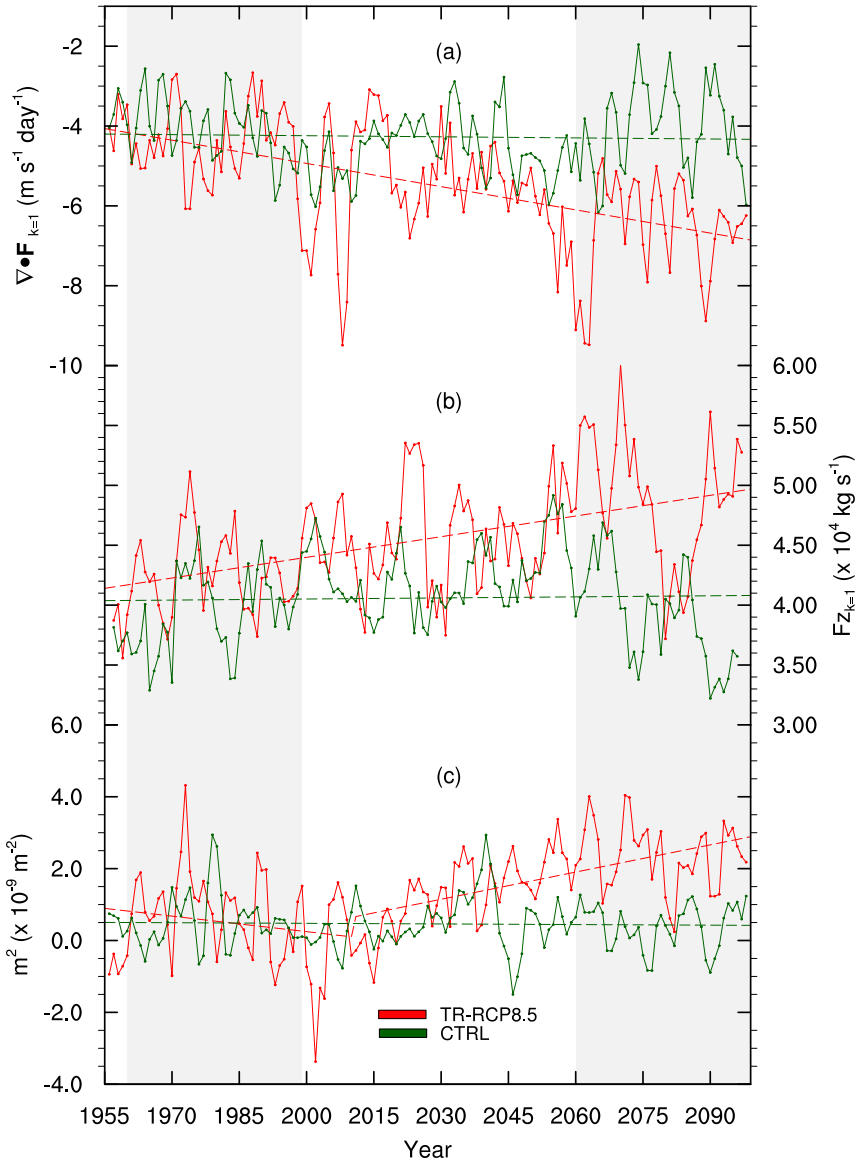

FIG. 5. Nov-Jan (NDJ) mean of (a) wave-1 EP-flux divergence averaged over 10-0.1 hPa and 60-80°N, (b) vertical component of EP-flux vectors at 100 hPa averaged over 40-70°N and (c) vertical wavenumbers averaged over 5-1 hPa and 60-80°N, from the TR-RCP8.5 (red) and CTRL (green) simulations. The straight dashed lines indicate linear best-fit regression (trend).

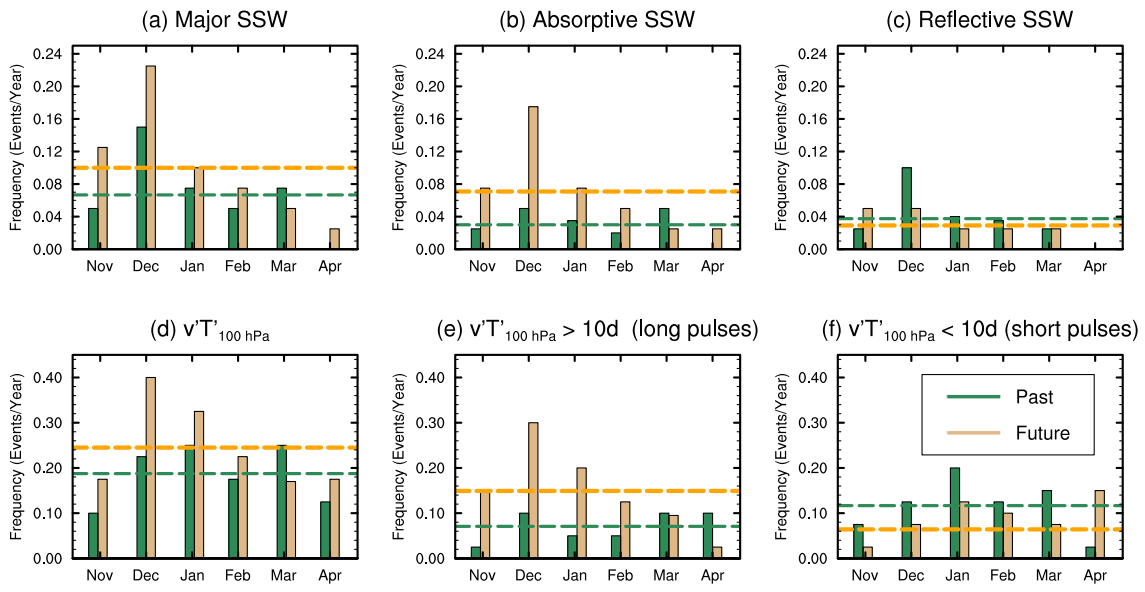

FIG. 6. The frequency of major warmings and upward heat flux events in NH winter months in TR-RCP8.5 simulation for the past (1960-1999, orange) and the future (2060-2099, dark-green). (a) total frequency of major warming events and their decomposition into (b) absorptive and (c) reflective events. (d) the frequency of upward heat flux ($\overline{v'T'}$ >0) events at 100 hPa and their decomposition into (e) upward waves with long pulses and (f) with short pulses. The horizontal dashed lines indicate the mean of the frequency.

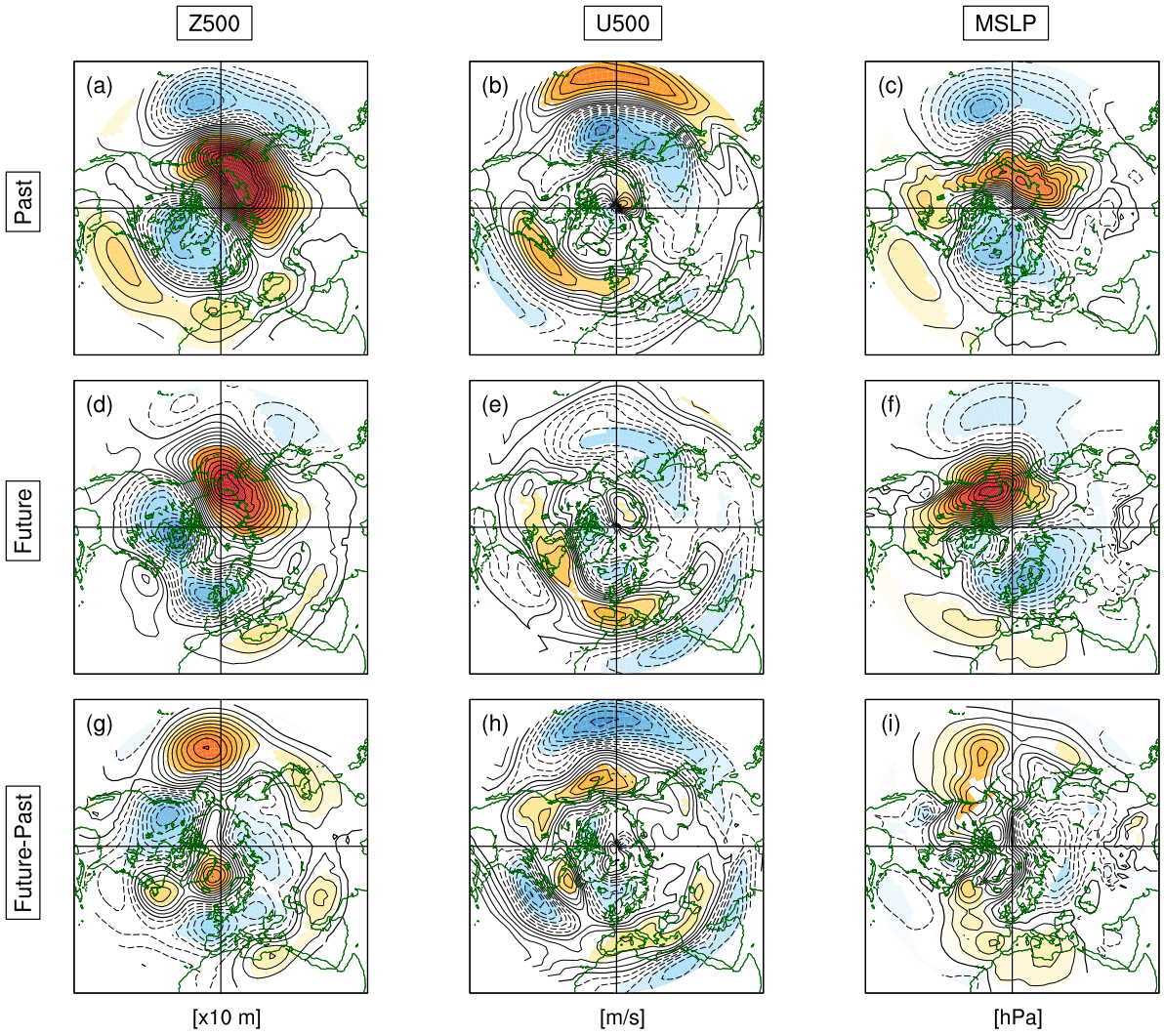

FIG. 7. The composites of (a,d) 500-hPa geopotential height (Z500), (b,e) 500-hPa zonal wind (U500), and (c,f) mean sea level pressure (MSLP) anomalies during the period of maximum DWC impact on the troposphere (days -3 to 3) in JFM for (top) TR-RCP8.5 past (1960-1999) and (bottom) TR-RCP8.5 future (2060-2099). (g-i) The difference between the future and the past of the respective anomalies. Contour interval is 10 m for Z500, 1 m/s for U500, and 1 hPa for MSLP. The zero contour is omitted. The color shadings are only drawn for anomalies that are statistically significant at the 95% confidence level according to a 1000-trial Monte Carlo test.

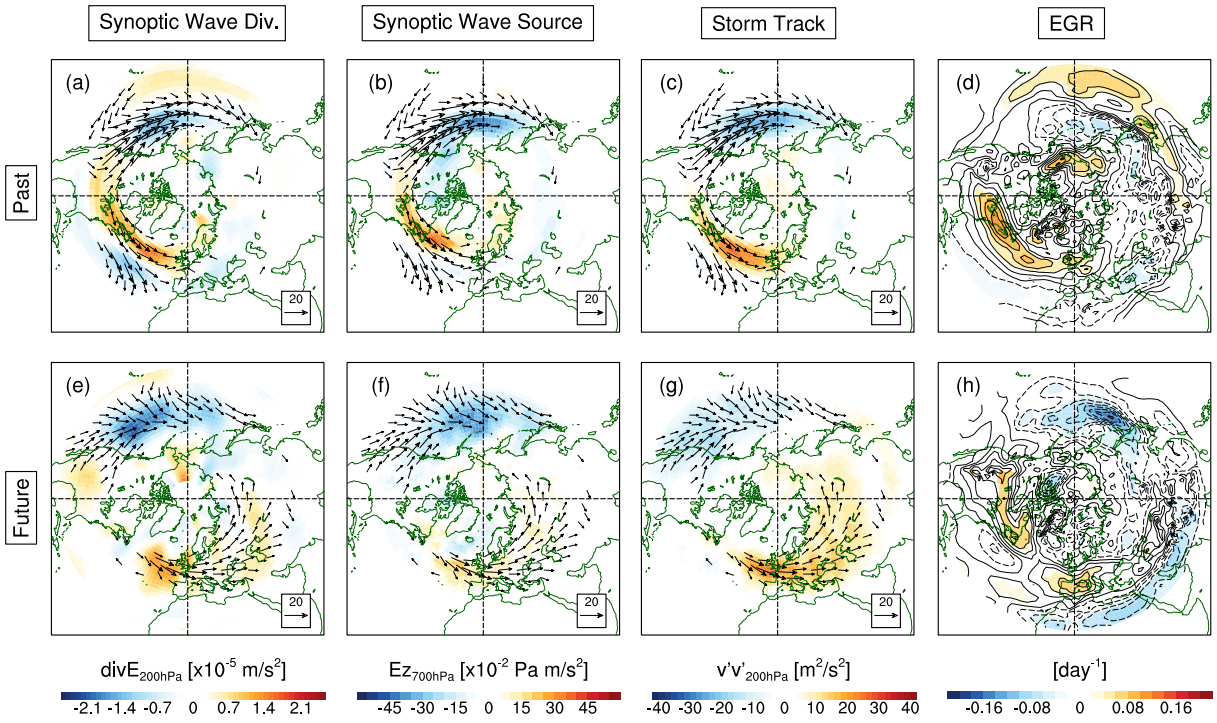

FIG. 8. The composites of (a,e) 200 hPa synoptic wave divergence, (b,f) 775 hPa synoptic wave source, (c,g) 200 hPa storm track, and (d,h) 700-hPa Eady's growth rate anomalies during the period of maximum DWC impact on the troposphere (days -3 to 3) in JFM, for (top) TR-RCP8.5 past (1960-1999) and (bottom) TR-RCP8.5 future (2060-2099). The vectors indicate horizontal component of **E** vectors (Fx, Fy) at 200 hPa. The vertical component of **E** vectors in (b,f) is calculated by $-f\overline{v'\theta'}(\partial\theta/\partial p)^{-1}$ representing the synoptic wave source, where the positive (negative) values indicate upward (downward) synoptic wave fluxes. The color shading in (c,g) indicates the upper-level storm track anomalies ($\overline{v'v'}$) at 200 hPa. The Eady maximum growth rate is calculated as $0.31|f||\partial u/\partial z|/N$. The shadings are only drawn for anomalies that are statistically significant at the 95% confidence level according to a 1000-trial Monte Carlo test.

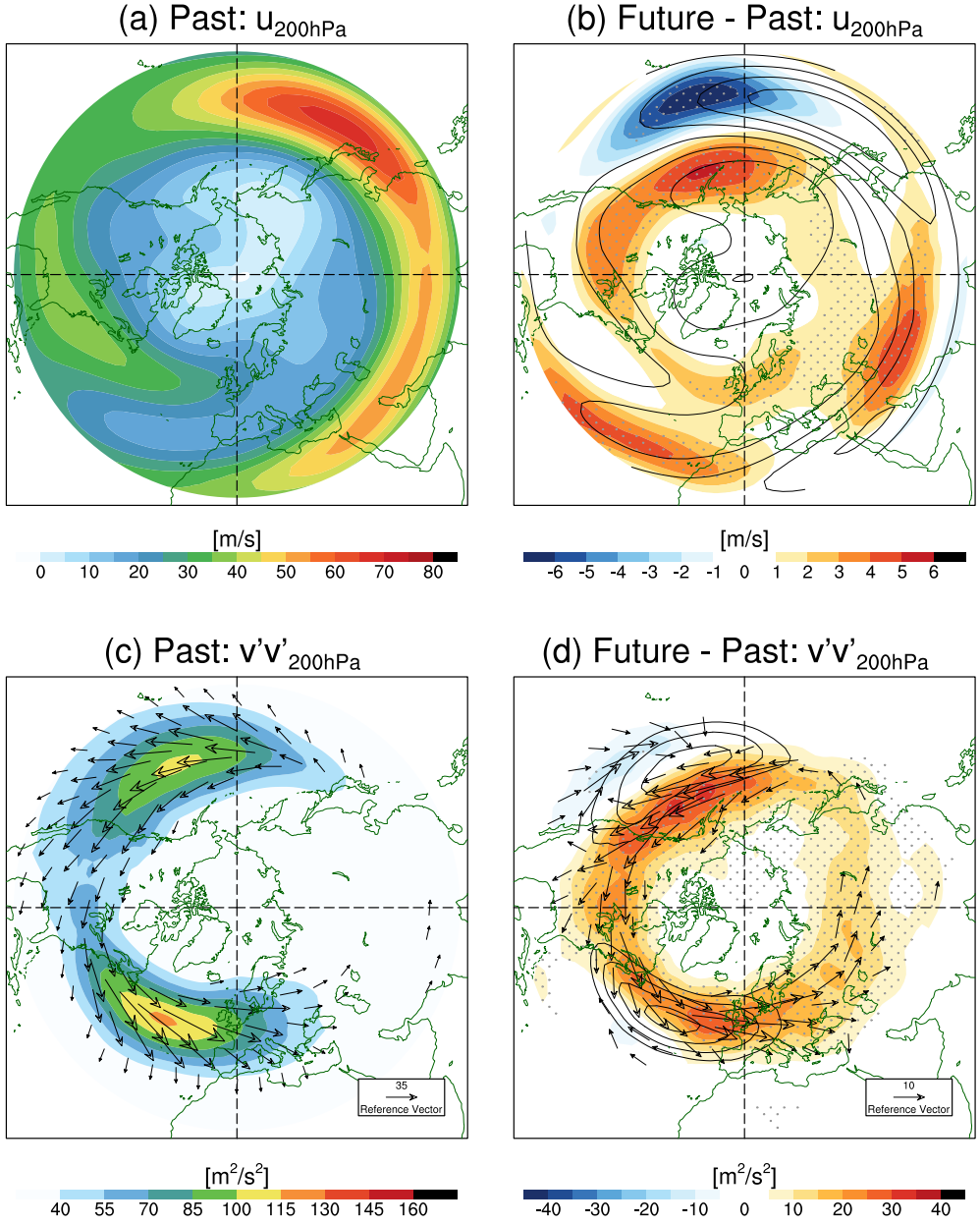

FIG. 9. Winter mean (JFM) 200-hPa zonal wind and 200-hPa storm track ($\overline{v'v'}$) from (a,c) the past and (b,d) the response (future-past) from RCP8.5 simulation (TR-RCP8.5). The black contour lines in (c,f) indicate a climatology from the past. The gray dots indicate the regions where the changes are significant at the 95% confidence level according to a two-tailed t test.

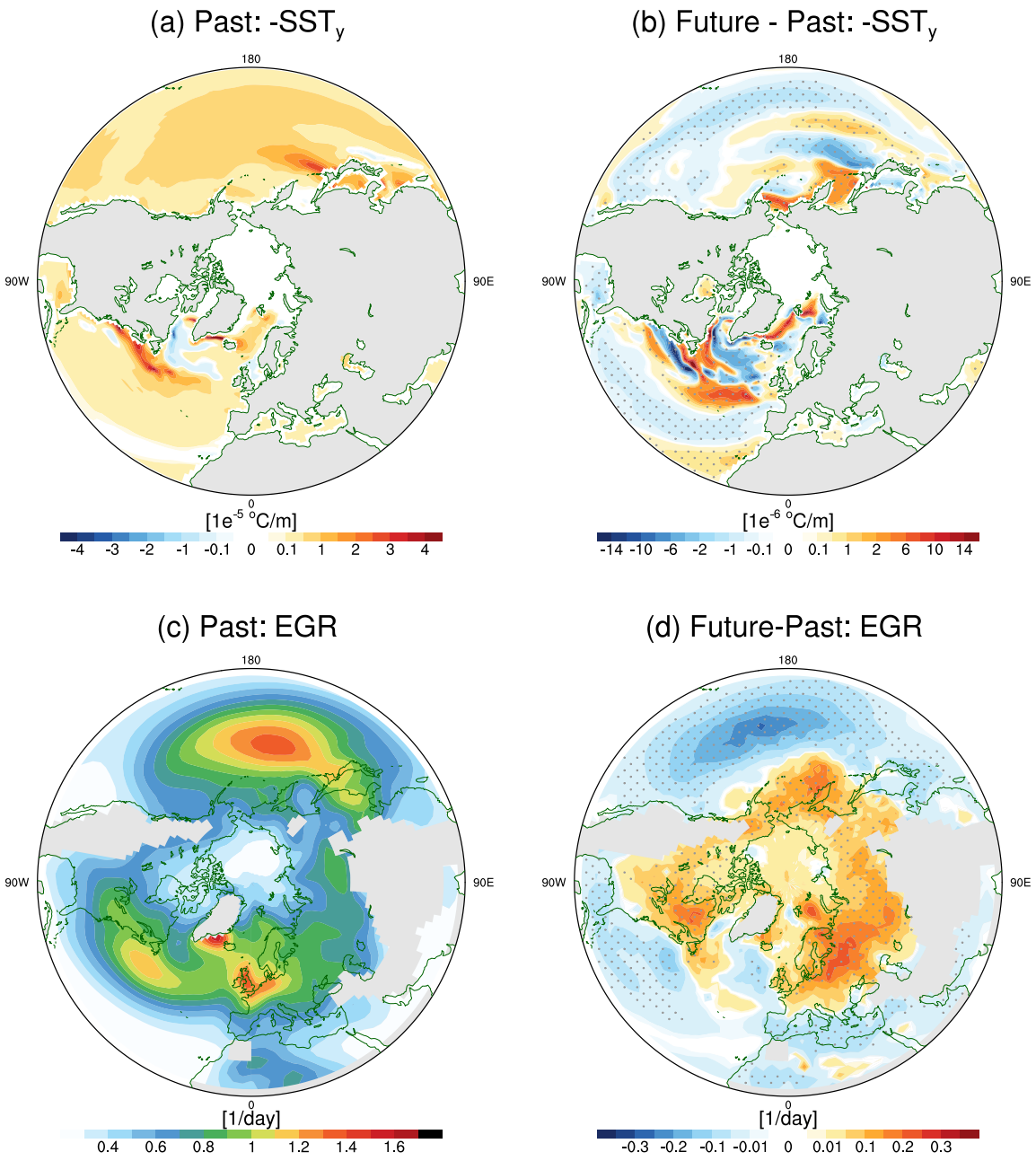

FIG. 10. Winter mean (JFM) meridional gradient of SST (SSTy) and Eady's growth rate maximum (EGR) at 925 hPa from (a,c) the past and (b,d) the response (future-past) in coupled RCP8.5 simulation (TR-RCP8.5). The gray shading regions indicate where the land or the "underground" grid points (i.e. z $>$ 1 km) have been excluded from the analysis. The SSTy value has been multiplied by minus one for a better comparison with the EGR's sign. The gray dots indicate the regions where the changes are significant at the 95% confidence level according to a two-tailed t test.